A Spectroscopic Survey of NGC6744

Amelia Sharp

A THESIS SUBMITTED IN PARTIAL FULFILMENT
OF THE REQUIREMENTS FOR THE DEGREE OF
MASTER OF SCIENCE

Jeremiah Horrocks Institute for Mathematics, Physics and Astronomy
University of Central Lancashire

June 2023

Declaration

Type of Award: Master of Science Master of Science

School: Natural Sciences

I declare that while registered as a candidate for the research degree, I have not been a registered candidate or enrolled student for another award of the University or other academic or professional institution.

I declare that the following material contained in the thesis formed part of a submission for the award of:

Bachelors of Science (Hons) in Astrophysics, University of Central Lancashire.

Table 3.3 (columns 4 and 5 only); Figures 4.1 and 4.2; Appendices A1, A2, and A3.

No proof-reading service was used in the compilation of this thesis.

Amelia Sharp

June 2023

Abstract

Cataloguing Wolf Rayet stars in galaxies within 30Mpc is vital for proving or disproving the theory that Wolf Rayet stars are progenitors of type Ib and Ic supernovae. I present a spectroscopic survey looking for Wolf Rayet stars in NGC6744. I used spectroscopy from the Gemini-South Multi Object Spectrograph to analyse 25 objects in a region in the South East of NGC 6744. These objects include candidate Wolf Rayet stars and HII regions. From this, I report spectroscopic confirmation of 35 Wolf-Rayet stars within 7 HeII emission-line sources, of which 17 have WC subtypes and 18 have WN subtypes. In addition, I present a new measurement for the metallicity gradient of NGC 6744 of $Log(O/H) + 12 = 8.73(\pm 0.06) - 0.30(\pm 0.06) \times R/R_{25}$ using strong line methods, where R/R_{25} is the fraction of the isophotal radius.

Contents

Acknowledgements

I would like to thank my supervisor, J. Pledger, for everything she has taught me this past year; for her feedback and advice; and for her patience and support. I would also like to thank M. Norris and A. Sansom for helping me when J. Pledger could not. I would like to thank my fellow UCLan research students for their support and encouragement; particularly Charlotte, Ethan, Josh, Matt, Simon and Ruth. Thank you for always humouring me when I make dumb jokes.

Chapter 1

Introduction

Over the past few decades the commonly held theory that Wolf Rayet (hereafter WR) stars undergo core collapse as type Ib or Ic supernovae has come into question, due a growing lack of clear WR progenitor star identifications. In order to investigate this theory more thoroughly, surveys of galaxies within 30Mpc have been undertaken to classify their WR content and serve as a catalogue for identifying the progenitor stars of future type Ib and Ic supernovae (which I will refer to as Ibc supernovae when referring to these two groups combined). I have undertaken a spectroscopic survey of NGC6744 to add to this catalogue and investigate metallicity in HII regions across the galaxy.

1.1 Wolf Rayet Stars

Classical WR stars are massive, evolved stars with stripped envelopes. They evolve from O stars of $20 M_{\odot}$ and above. Generally, theory focuses on single star scenarios where the stripping of the envelope is facilitated by strong stellar winds. These winds are optically thick and the gas they expel from the envelope forms an extended ionised region around the star. The spectra of these stars feature broad helium emission lines from the surface of the core, which has been revealed through removal of the hydrogen envelope (Crowther, 2007).

There are 2 main categories of non-classical WR star. The first occurs in interacting binary systems. These stars strip their envelopes through interactions such as Roche lobe overflow. This case will be discussed in Section 1.1.4. The second category of non-classical WR star are extremely massive stars that display helium emission and hydrogen emission while still on the main sequence. These are thought to still be hydrogen core-burning and have WR features due to extreme wind speeds (Yusof et al., 2013). As they have not evolved off the main sequence, these are not true WR stars.

1.1.1 WR Evolution

The current theory most widely accepted for the evolution of WR stars is called the Conti Scenario. First proposed in Conti (1975) and revised versions presented in Maeder & Conti (1994) and Maeder (1996), the theory states that post Main Sequence O stars evolve through various stages including some or all of Blue Supergiant (BSG); Red Supergiant (RSG); Large Blue Variable (LBV); and WR stages before undergoing core collapse as supernovae. Different initial masses of star result in different evolutionary pathways, as shown in Figure 1.1. The Conti Scenario, therefore, explains why some O stars display WR features and why some WN stars display WC features; these stars are all at different stages of the same evolutionary pathways.

There are 3 main subtypes of WR star: WN, WC and WO. These are identified by their nitrogen, carbon and oxygen emission lines, respectively. These elements are products of hydrogen burning within the star's core. Alongside helium emission, WN stars display evidence of their previous core hydrogen burning that has been revealed with the removal of the envelope, primarily in their nitrogen abundances. WC stars display evidence of core helium burning in the carbon abundances(Smith & Willis, 1982). Additionally, there is a group of WN stars with strong carbon features; these are considered to be stars transitioning between WN and WC stages and are called WN/C stars (Maeder & Conti, 1994). The strongest optical lines in WC spectra are generally broader than those in WN spectra. This

$\mathbf{M \geq 60\ M_{\odot}}$
$\mathrm{O \rightarrow Of \rightarrow WNL + abs \rightarrow WN7 \rightarrow (WNE) \rightarrow WCL \rightarrow WCE \rightarrow SN}$
$\mathrm{At\ low\ Z: \ldots WN7 \rightarrow WCE \rightarrow SN}$

$\mathbf{M \simeq 40\text{–}60\ M_{\odot}}$
$\mathrm{O \rightarrow Of \rightarrow LBV \rightarrow WN8 \rightarrow WNE \rightarrow WCE \rightarrow SN}$

$\mathbf{M \simeq 25\text{–}40\ M_{\odot}}$
$\mathrm{O \rightarrow (BSG) \rightarrow RSG \rightarrow (BSG) \rightarrow WNE \rightarrow (WCE) \rightarrow SN}$

Figure 1.1: The Conti scenario for evolutionary pathways of WR stars of different initial masses (Maeder, 1996).

makes them easier to identify in data with high foreground extinction. Additionally, WN stars with higher luminosity tend to have weaker emission lines due to them having larger amounts of hydrogen remaining Crowther (2007). Both of these characteristics lead to an observational bias towards WC stars in interference filter imaging surveys.

The subtypes of WR star are also subdivided into numbered excitation types. Stars are sorted into these types based on the ratios of emission lines apparent in their spectra (Crowther et al. 1998; Smith et al. 1994; Smith et al. 1996). WN types are numbered from 2 to 11, WC from 4 to 9 and WO from 1 to 4. Early type and late type categorisation of WR stars relates to their excitation. Early type (E) being the high excitation group and late type (L) being the low excitation group (van der Hucht et al., 1981). In other words, early type WR stars have higher temperatures and therefore exhibit higher ionisation levels.

1.1.2 WR Winds

WR stars have powerful winds which create their characteristic spectra. These were first theorised in 1929 (Beals, 1929) and subsequently observed in 1967 (Morton, 1967). These winds are radiatively driven by pressure from photons within the stellar atmosphere. The commonly accepted model for this process is that presented in Castor et al. (1975), who

showed theoretically that the force from emission lines within the star could create stellar winds strong enough to strip the stellar envelope from a high mass star. The WR star with the most powerful known winds has winds of velocity $5750 kms^{-1}$ (Drew et al., 2004). However, more usually WR stars display wind velocities between 700 and 2200 km/s. For a full table of average wind velocities for each WR subtype see Table 2 in Crowther (2007) which compiles wind velocities from Herald et al. (1999); Crowther et al. (2002); Barniske et al. (2006); Crowther et al. (2006); and Hamann et al. (2006).

Moens et al. (2022) have recently shown that a two-part mechanism can be used to recreate WR-style winds in a 3D numerical model. This model uses radiation driven winds close to the stellar core that transition to line driven winds further out. They suggest that the boundary point where a star transitions from optically thin to optically thick winds occurs at $\frac{L_*}{L_{Edd}} \approx 0.4$. In other words, the transition point from optically thin to optically thick winds for helium stars occurs when the stellar luminosity is $\geq 40\%$ of the Eddington luminosity.

1.1.3 Metallicity Dependence

The WR stellar winds are theoretically metallicity dependent. Within a lower metallicity environment (i.e. the Small Magellanic Cloud) fewer stars enter the WR phase compared to a solar or super-solar metallicity environment. This is because at higher metallicities, the stellar winds that strip the hydrogen envelope can occur in stars which have a lower initial mass. These strong stellar winds begin at lower initial mass when there is more iron within the atmosphere of the star (Sander, 2022; Vink, 2022).

The ratio of WN to WC and WO stars is also metallicity dependent: The initial mass required for a star to evolve to carbon and oxygen burning decreases as metallicity increases (Aguilera-Dena et al., 2022). The strong stellar winds which create the WR spectrum activate at a lower initial mass when the star is formed in a higher metallicity environment.

However, Shenar et al. (2020) show that the binary fraction of WR stars is metallicity

independent, suggesting that both WN and WC stars are affected equally by binary interactions. This implies that initial mass is the strongest factor in deciding the subtype of WR stars, regardless of whether they are single star or multiple star systems.

1.1.4 Binarity

While it is known a certain percentage of WR stars are in binary systems and a different percentage will interact, the effects of these are difficult to determine. Dsilva et al. (2020, 2022) find the binary fraction of galactic WR stars to be dependent on subtype, with WC stars generally having a binary fraction of $0.96^{+0.04}_{-0.22}$ and long periods; and WNE stars generally having a binary fraction $0.56^{+0.20}_{-0.15}$ and short periods.

Sana et al. (2012) predict that 70% of stars that are initially O-type will interact with a companion and 40-50% will either be stripped of their envelope or accrete significant mass during these interactions. Sana et al. (2012) also find that 33% of initially O-type stars are stripped enough through interactions to undergo core collapse as hydrogen deficient type Ibc or type IIb supernovae. Whether or not all WR stars have or will interact with a binary companion, binary interaction clearly has some impact on massive star evolution.

On the other hand, Shenar et al. (2020) argue that envelope stripping on its own is not enough to result in a WR spectrum. Indeed, in order to display the broad emission lines characteristic of a WR star, the star must have both a stripped envelope as well as powerful stellar winds. Stars with only a stripped envelope and no winds will not have WR spectra. For example, a hot subdwarf star which lost its hydrogen envelope in a commmon envelope phase would be a stripped envelope helium star without the characteristic WR winds (Saffer et al., 1994; Han et al., 2010).

1.1.5 Supernova Progenitors

Type Ib and Ic supernovae lack either hydrogen or both hydrogen and helium in their spectra, respectively. For this reason, WR stars are considered potential type Ibc supernova progenitors. In Fig.1.2 it is shown how stripped envelope stars can correspond to hydrogen-deficient supernova spectra. Fig.1.3 shows that WR stars have large enough initial mass to form a type Ibc supernova upon core collapse.

Heger et al. (2003) used non-rotating models of single stars between $9M_{\odot}$ and $300M_{\odot}$ and evolved them to find their remnants (see Fig.1.4) and supernova properties (see Fig. 1.3). They assumed that stars with a final mass $< 65M_{\odot}$ underwent core collapse and those with $65M_{\odot} - 135M_{\odot}$ underwent pair instability collapse. Under these circumstances, the figures show that for massive stars at low metallicity with no hydrogen envelope the majority of remnants should be black holes, and therefore invisible to direct observation. This changes at higher metallicity with neutron star remnants dominating.

Direct observational evidence for WR progenitors is lacking (Eldridge et al., 2013; Van Dyk, 2017). Supernovae are much brighter than individual stars and so can be detected at much greater distances where progenitor stars are undetectable. Additionally, where progenitor stars have been identified in pre-supernova imaging it is difficult to confirm they are a WR star due to a lack of spectroscopy.

For some supernovae, such as type Ib supernovae iPTF13bvn and 2019yvr, the data available supports a helium star in a binary system (Cao et al., 2013; Eldridge & Maund, 2016; Kilpatrick et al., 2021). Other supernovae have confirmed progenitors that do not fit known WR models such as type Ic supernova 2017ein (Kilpatrick et al., 2018; Dyk et al., 2018). Alternatively, where supernova characteristics do support a WR progenitor no progenitor has been identified in pre-imaging, preventing the confirmation of the hypothesis (Gal-Yam et al., 2022).

In particular, SN iPTF13bvn is interesting because of the breadth of investigation and conclusions drawn from it. Cao et al. (2013) use archival HST imaging to derive colour and

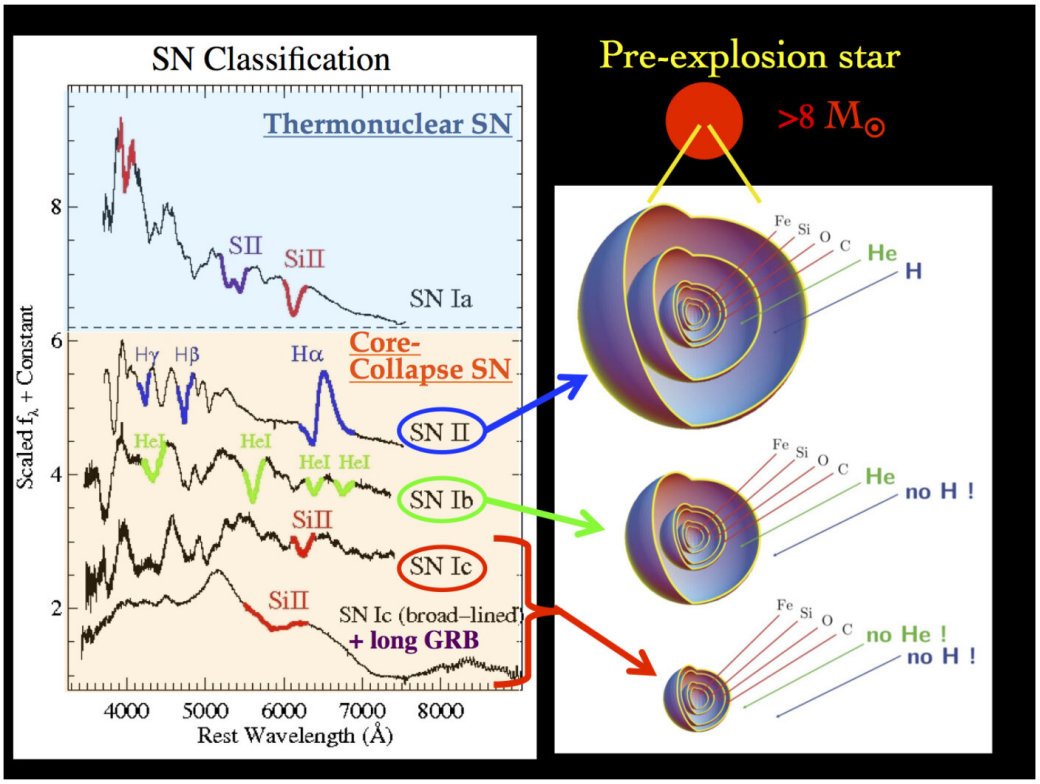

Figure 1.2: Graphic comparing example supernova spectra with the theoretical shell structure of 3 types of evolved star to show how the spectral features may be formed (Modjaz, 2011)

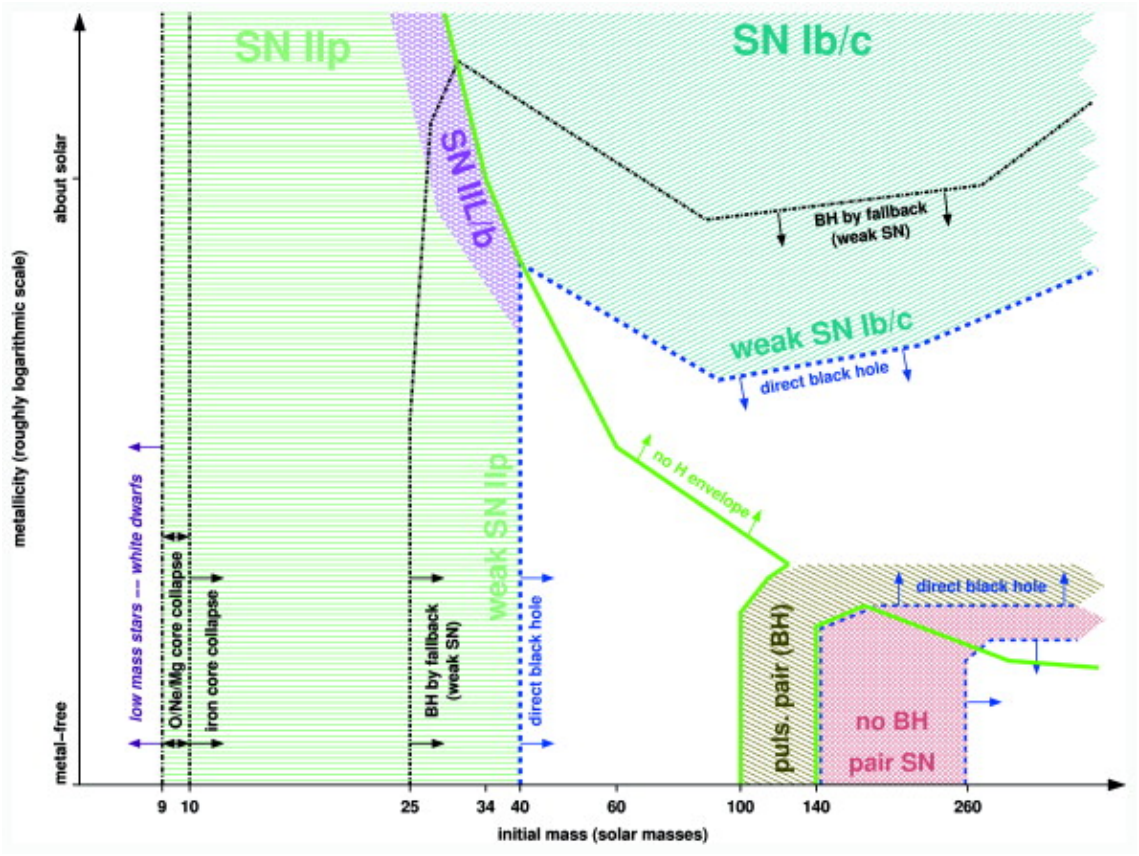

Figure 1.3: Plot of initial mass against metallicity and showing the different supernova outcomes in different parts of the frame. Type Ibc supernovae require both high metallicity and high initial mass (Heger et al., 2003).

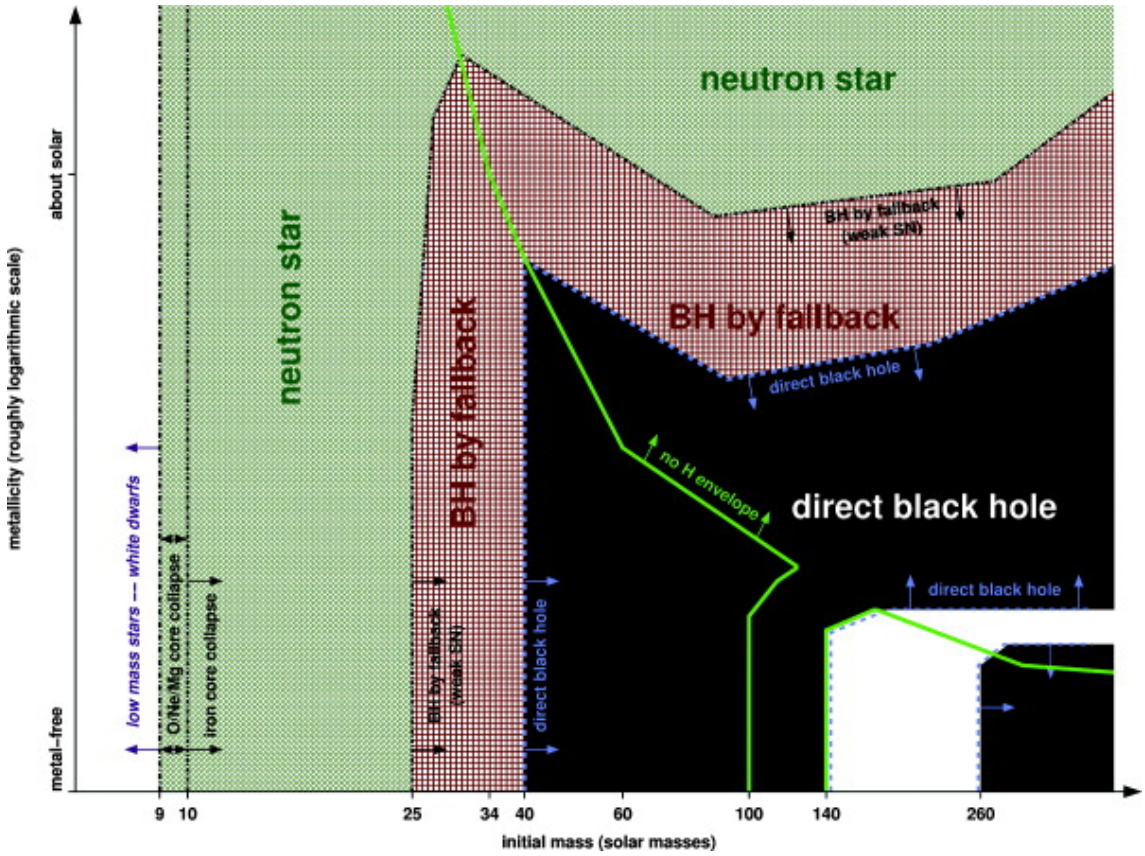

Figure 1.4: A plot of initial mass against metallicity showing the required characteristics to form a black hole or a neutron star after core collapse (Heger et al., 2003).

luminosity for an identified progenitor star and concluded these properties were consistent with a WR star. Groh et al. (2013) used Geneva single star models to predict the progenitor properties and found them consistent with a massive, single star, but the predicted ejecta mass derived was too high. In contrast, Bersten et al. (2014) find the progenitor to be consistent with a binary star system using their models.

For supernovae occurring in galaxies that have been observed before, progenitor identification is done by analysing pre-supernova imaging. Some supernovae have pre-imaging that can be used to investigate their progenitor properties (Eldridge et al., 2013). However, the depth of the pre-supernova imaging can be inaccurate in regards to WR stars as the effect of line dilution and absorption from the surrounding stellar population can mask WR emission lines (Pledger et al., 2021). Therefore, WR stars can evade detection even in imaging which is otherwise good enough to detect them.

1.1.6 WR Surveys

Since the first WR stars were identified in 1867 there have been various attempts to catalogue them both within and without the Milky Way. For WR stars within the Galaxy, the most recently published full catalogue was van der Hucht (2001) though there have been many subsequent individual discoveries bringing the number of known WR stars in the galaxy to 667 [1].

For WR stars outside of the galaxy, there have been several surveys. Of particular interest are the surveys of the spiral galaxies NGC 5068, with 32 confirmed WR stars, (Bibby & Crowther, 2012) and M101, with an initial 10 confirmed WR stars (Shara et al., 2013,Pledger et al., 2018). Further surveys are referenced within (Hadfield & Crowther, 2008) and (Neugent & Massey, 2019), however, it is beyond the scope of this work to compare all of them.

[1] An up to date catalogue is maintained by Prof. Crowther at https://pacrowther.staff.shef.ac.uk/WRcat/index.php

Table 1.1: Properties of NGC6744 according to literature.

Property	Value	Reference
RA	19h09m41s	Koribalski et al. (2004)
Dec	-63d51'47"	Koribalski et al. (2004)
Distance	9.39±0.43Mpc	Anand et al. (2021)
Metallicity	8.75 (±0.04)*	Pilyugin et al. (2006)
Inclination	53±2 deg	Lang et al. (2020)
Position Angle	14.0±0.2 deg	Lang et al. (2020)
Structure	SAB(r)bc	de Vaucouleurs et al. (1991)
Stellar Mass	$2.2E^{10}M_{\odot}$	Sabbi et al. (2018)

*Found from the least squares fit to a plot of Log (O/H) + 12 metallicity distribution

1.2 NGC6744

NGC6744 is an isolated galaxy at 9.4 ± 0.4 Mpc (Anand et al., 2021) with a single dwarf galaxy companion NGC6744a (Yew et al., 2018). Ryder (1995) found it to have a particularly steep metallicity gradient, with values of 12+Log(O/H) $>$ 9.2 in the center of the galaxy and $<$ 8.5 in the furthest parts of the spiral arms where O/H is the number of oxygen atoms per hydrogen atom.

NGC6744 has been described as a Milky Way twin due to its flocculent spiral arms and its slightly extended bulge, though the Milky Way has a more peanut shaped bulge (Yew et al., 2018). Silva et al. (2018) studied emitting regions in NGC6744 which they attribute to ionisation from the jets of a low luminosity AGN, a feature corroborated by Yew et al. (2018). Yew et al. (2018) discovered 2 supernova remnants; 5 candidate supernova remnants; and calculated a Star Formation Rate (SFR) of $2.8 - 4.7 M_{\odot} yr^{-1}$. This agrees within error with the SFR of $3.15 M_{\odot} yr^{-1}$ found by using the flux data from (Kennicutt et al., 2008) and the method described in (Kennicutt, 1998).

Figure 1.5: A broad band image of NGC6744 taken with the ESO DanishB Telescope in the B-band filter (Larsen & Richtler, 1999). It is oriented North up and East left. The Field of View (FoV) is 13.7' x 13.7'.

1.2.1 SN 2005at

In 2005 a type Ic supernova was observed in NGC6744. There is a single paper investigating its properties from Kankare et al. (2014) who are unable place hard limits upon the progenitor's characteristics because all but 3 epochs of the original observations at Bronberg Observatory have been lost. However, various late time observations are still available. They note that extinction in the environment of SN 2005 at is high, $A_v = 1.9 \pm 0.1$mag, which is likely due to the high amounts of dust in NGC6744. Kankare et al. also discover a potential WR cluster within $0.22''$ of the SN position in pre and post supernova imaging.

No other supernova has been observed in NGC6744 since 2005, though Yew et al. (2018) found evidence of older supernova remnants.

1.3 Motivation

Pre-supernova imaging is vital for correctly identifying a supernova progenitor, however, broad-band imaging does not allow for identification of WR stars due to the dilution of the emission lines. This means that most pre-supernova imaging is unable to determine if a progenitor has WR properties. In order to test the theory regarding Type Ibc supernova progenitors, a catalogue of WR stars in galaxies where the properties of WR stars may be directly measured is the most effective method. Given that the WR phase generally lasts for 0.5Myr, the assumption is that in order to observe one going supernova within a 5 year period, and therefore confirm the type Ibc progenitor scenario, a catalogue of at least 100'000 WR stars is needed.

This work adds to the body of WR surveys discussed in Section 1.1.6. In addition, this work presents metallicities and fluxes for the target regions.

Chapter 2

Method

2.1 Multi-Object Spectroscopy

2.1.1 Data Collection

The spectral data were taken over the period of 13.06.2009 to 24.08.2009 under project ID GS-2009A-Q-20 (PI: Paul Crowther) using the Gemini Multi Object Spectrograph (henceforth GMOS) at the Gemini-South telescope. They are available from the Gemini Science Archive [1]. The data contains 6 MOS masks in total, with the masks 4, 5 and 6 targeting NGC6744 and masks 1, 2 and 3 targeting NGC5068. There are a total of 84 targets within NGC6744. In this work I reduced one mask, Mask 05.

WR candidates were chosen by comparing Very Large Telescope (VLT) data taken with the FOcal Reducer and low dispersion Spectrograph (FORS1). These images were taken in narrow band filters focused on λ4686 and λ4750. The continuum filter, λ4750, was subtracted from the HeII filter, λ4686, to highlight HeII emission line sources which were then analysed to find candidate WR stars. The WR candidates display a wide range of magnitudes, some sources required long exposures and others much shorter ones. Therefore, the brighter sources were imaged in Masks 4 and 6 and the fainter sources in Mask

[1] https://archive.gemini.edu/searchform/GS-2009A-Q-20

Table 2.1: This Table shows the number of targets, exposure time and region targeted by each mask and the coordinates and exposure time of each standard star.

Object	Mask	Region	Exposure Time (s)	No. Targets
NGC 6744	Mask 4	South East	430 x 2	26
	Mask 5	South East	1400 x 2	28
	Mask 6	North West	430 x 2	30
Object	RA	Dec	Exposure Time (s)	Candidates
EG21	3h 10m 30.9s	-68:36:02.20	30	Standard Star
LTT1020	1h 54m 50.2s	-27:28:35.70	120	Standard Star

5. Mask 4 and Mask 5 observed targets in the South East region of the galaxy and Mask 6 observed the North West region.

Some of the science targets are HII regions that were selected in order to calculate the metallicity across the galaxy and fill out the spaces in the mask. In addition, three of the slits on each mask were used for accurate position finding. These slits are not counted in the total targets list. The slits on science targets were 1" in width.

For each mask, the galaxy was observed at two central wavelengths, 510nm and 530nm. The Gemini-South telescope was fitted with the EEV CCD, at the time, which was made up of 3 chips and thus had 2 chip gaps. The two offset central wavelengths were used to cover the extent of these chip gaps in case any diagnostic emission lines fell in that region.

Masks 4 and 6 have 2 exposures, one for each central wavelength (see Table 2.1). Mask 5 was observed on an additional evening which means it has an additional exposure available, however, the seeing deteriorated quickly on that evening which prevented further observations.

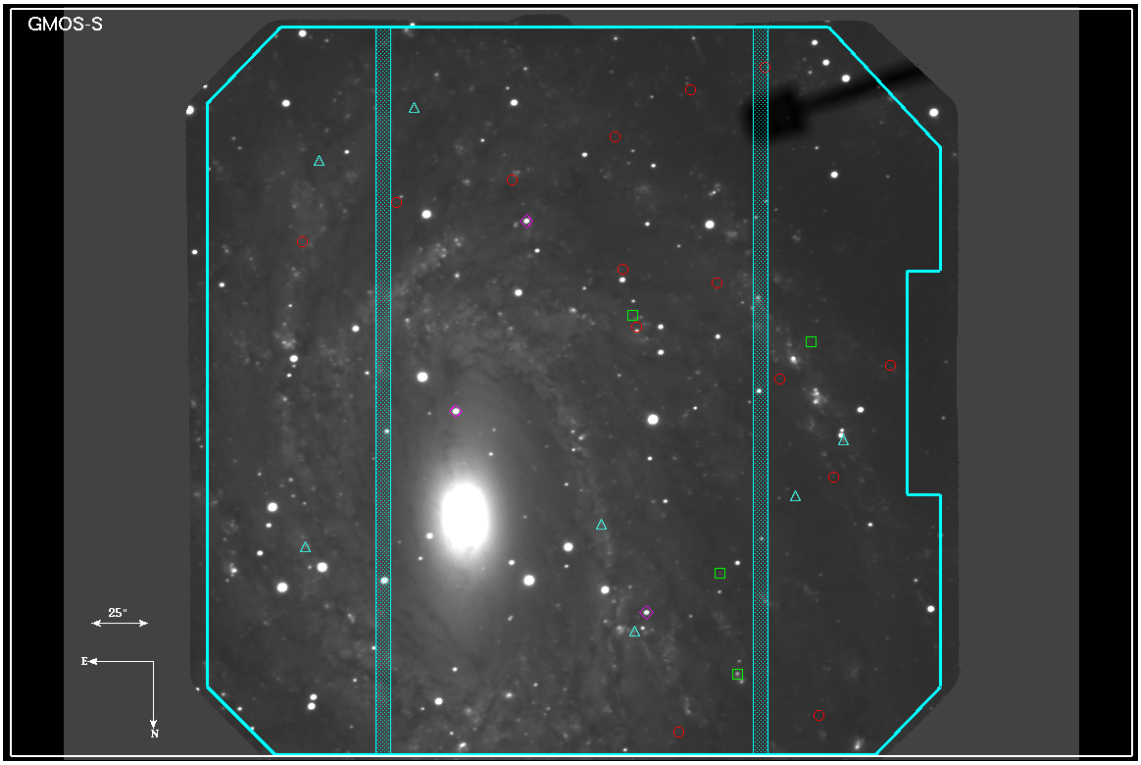

Figure 2.1: g-filter GMOS pre-imaging of NGC 6744 with the finding chart overplotted. It shows the 25 science targets, 3 finding stars and the two chip gaps. The chip gaps are shaded in blue and the finding stars are indicated by pink diamonds. Red circles show the highest priority candidates (the faintest WR stars), blue triangles the medium priority and green squares the lowest priority.

2.1.2 Data Reduction

Bias Subtraction

Zero time exposures with no illumination are taken throughout the observing run as part of normal operating procedure. These exposures are called bias frames and are used to remove the bias level added prevent negative pixels in the image when read out from the instrument. A mean bias image was created for each observing night by combining the bias frames taken over the evening using the Gemini IRAF GBIAS routine. There were a large quantity of images so I created lists of the relevant filenames using the IRAF HSELECT command. These lists of image names were then written to text files and used to automate creating the bias frames. These combined bias images are then subtracted from the science images.

Flat Field

The GCAL instrument is used to create evenly illuminated but featureless images that are used to calculate the response to light across the telescope detectors. These is used to remove the effects of dust and other imperfections from the science images. These exposures are called flat fields. A flat field image was taken for each of the two central wavelengths on each observing night. I used the Gemini IRAF GSFLAT routine on these flat field images to create calibration files. In order to create an effective calibration GSFLAT was run interactively so that the order of the fit could be adjusted (see Figs 2.2 and 2.3). Where the dashed line followed the solid line, the fit was good. I aimed for the lowest order of fit possible, which was generally between 15 and 25. The science data was divided by the flat field calibration to remove the artefacts from across the CCD.

Extraction

Once the bias and flat field calibration images were created, I then reduced the data using the Gemini IRAF GSREDUCE routine. This applied the bias, flat field and gain corrections.

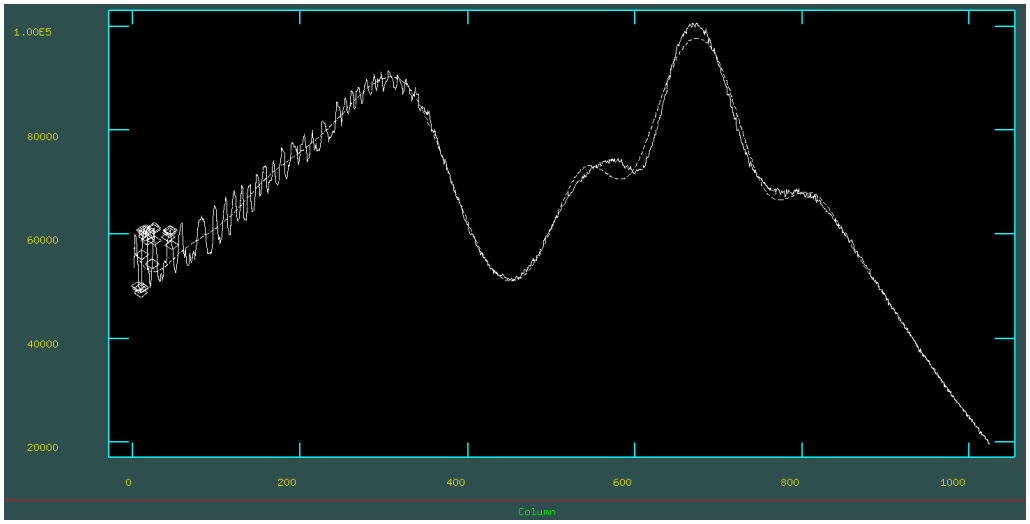

Figure 2.2: This figure shows a poor fit to the flat field being calibrated with GSFLAT with the solid line plotting the data and the dotted line plotting the fit. The low order of fit underestimates the local maxima which results in part of the fit being plotted to the left of the actual data.

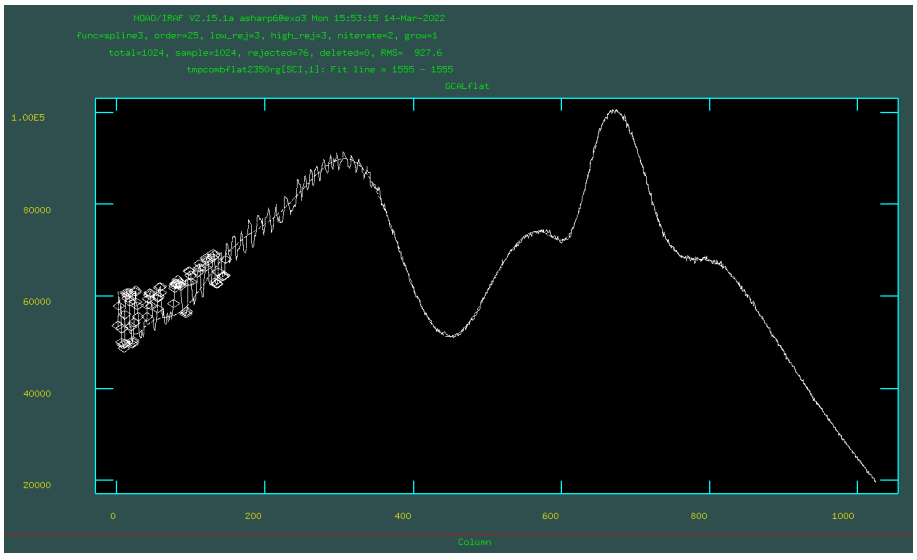

Figure 2.3: Fitting the flat field correction with GSFLAT. The dotted line shows the fit and the solid line shows the data. The left side of the spectrum has large amounts of noise from second order contamination.

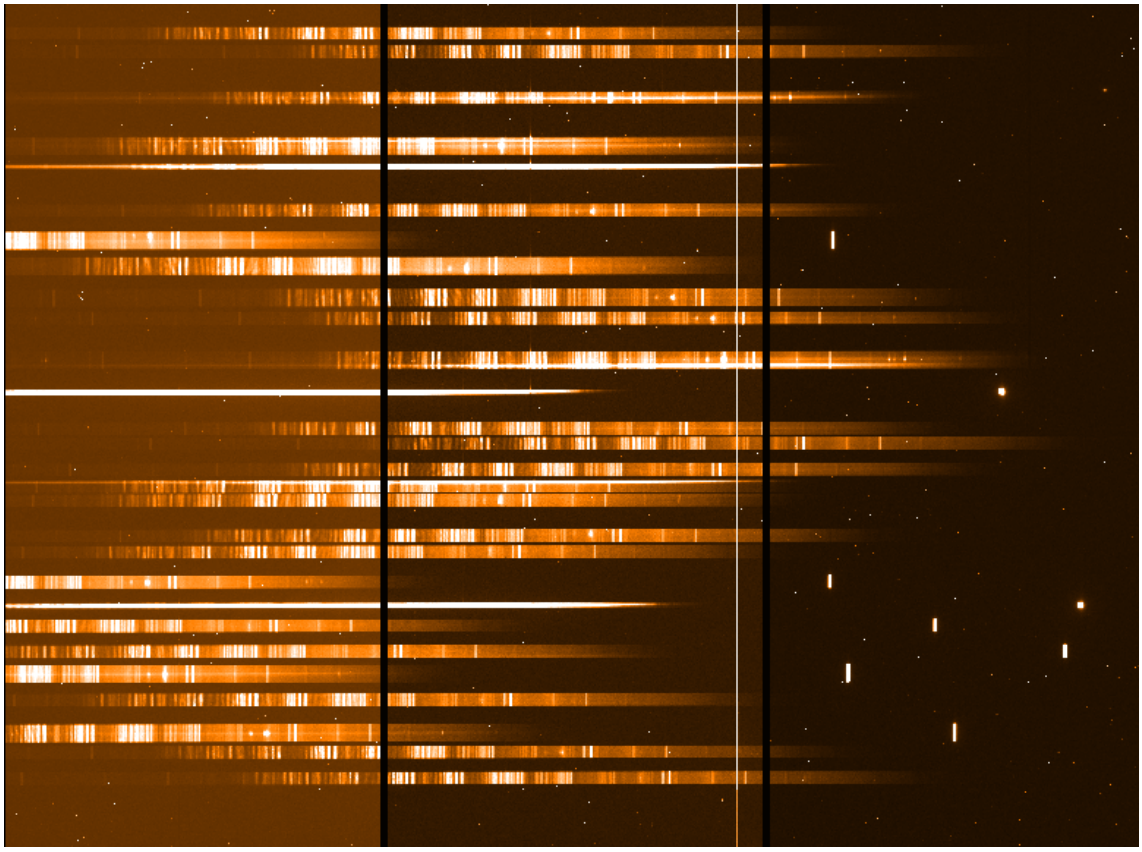

Figure 2.4: This figure shows the 530nm central wavelength images from each of the three chips on the GMOS CCD combined into one image. Each horizontal strip in the image is a spectrum before it has been extracted. The two black vertical lines are the chip gaps.

GSREDUCE also calls the GMOSAIC and GSCUT routines to combine the 3 chips of the CCD (see Fig 2.4) and cut the resulting image into slits according to the Mask Definition File (MDF) (see Fig. 2.1). The slits were extracted using the NOAO IRAF TWODSPEC APALL routine. To do this, I identified a visually bright feature in each spectrum and used its x pixel co-ordinates to select it within the APALL routine window (see Fig 2.5a). Then I adjusted the width of the extraction area so that it fit the feature and identified areas to use as background (see Fig 2.5b). The fit to the data is also adjusted interactively (see Figs 2.5c, 2.5d). An example output spectrum is shown in Fig 2.5e. Only the science spectra and standard star spectra were background subtracted; the calibration spectra were not.

Wavelength Calibration

In addition to bias subtraction and flat fielding, the data must be calibrated to ensure the pixels of the spectrum correlate with the correct wavelength. This is done by comparing a spectrum of a lamp with well known emission lines with that of the science data. These known lines can then be matched to those in the science data and used to convert the pixel scale to Angstroms. For the GMOS-S instrument the lamp used is a CuAr arc lamp.

Initially, I planned to wavelength calibrate the data before extracting it, however, the GSWAVELENGTH routine in the Gemini IRAF package does not run when the data input have different dimensions, which was a problem I did not have time to solve. Therefore, I used the NOAO IRAF APALL routine to extract the spectra first and then used the IDENTIFY and DISPCOR routines to apply the calibration.

I identified the emission lines in the CuAr arcs by eye, comparing to the standard line pattern for the grating used provided to me by my supervisor. Once these lines were identified, the IDENTIFY routine calculated the offset between the pixel scale and Angstroms to create the wavelength calibration. For the science data, I repeated this process but using the REIDENTIFY routine, which runs the identify routine with another spectrum as a reference. For my reference spectra I used the arc extracted from the same slit as the spectrum

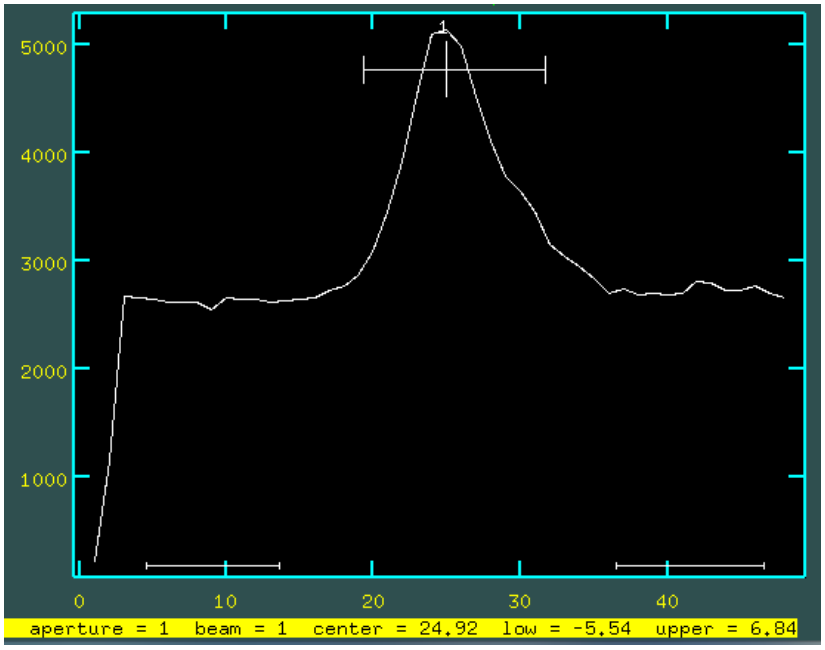

(a) This figure shows a feature to be extracted using APALL. The horizontal bar shows the upper and lower selection limits. The y axis is measured in counts and the x axis in pixels.

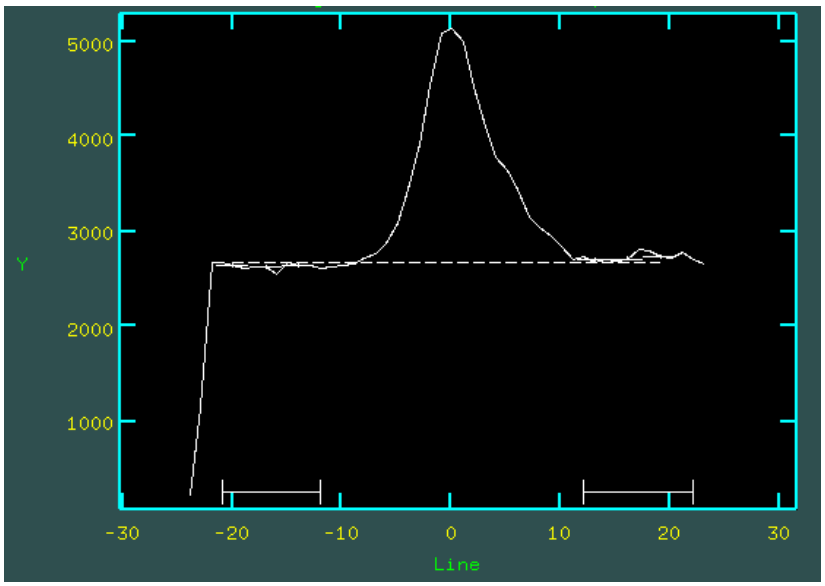

(b) The bars at the bottom of the plot show the areas selected for use as background. The y axis is measured in counts and the x axis in pixels. The dashed line shows the calculated background level.

Figure 2.5: The interactive steps in APALL to extract a spectrum.

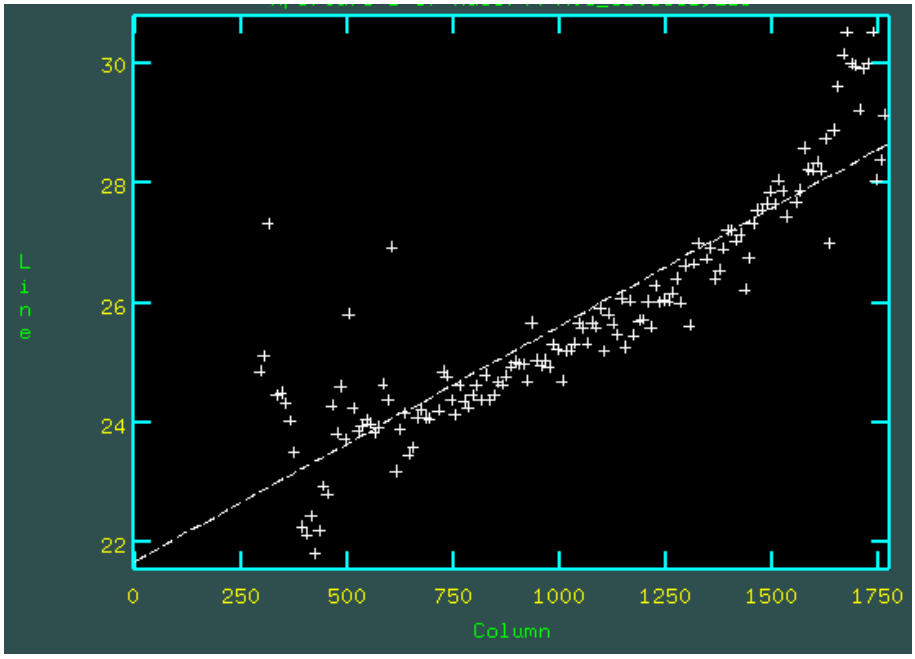

(c) The scatter points show the data and the dotted white line shows a 2nd order fit. This fit does not follow the data well.

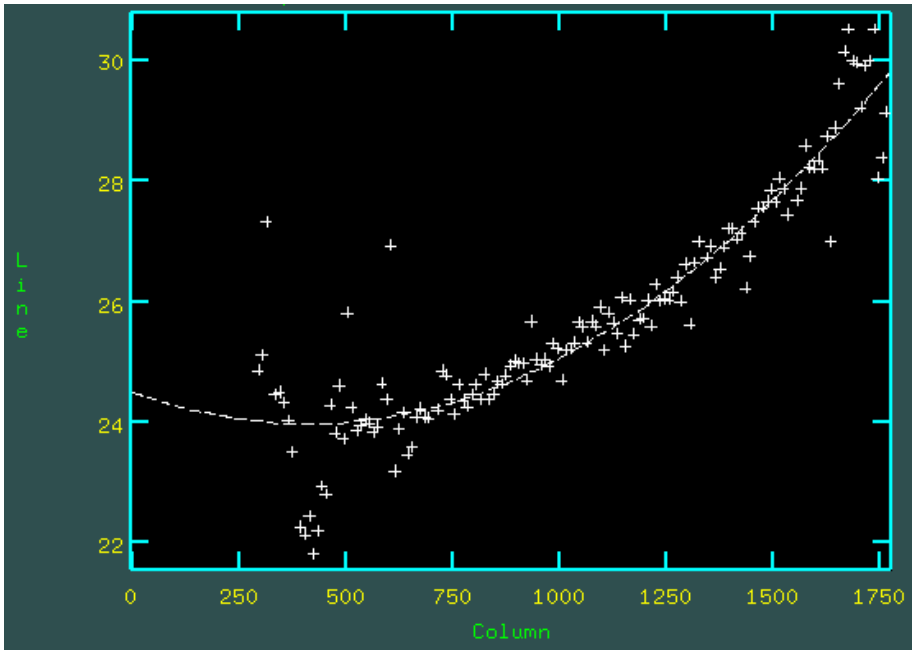

(d) The scatter points show the data. In this figure the dotted line shows a 3rd order fit to the data which visibly follows the data points much more closely than in Fig. 2.5c.

Figure 2.5: The interactive steps steps in APALL to extract a spectrum.

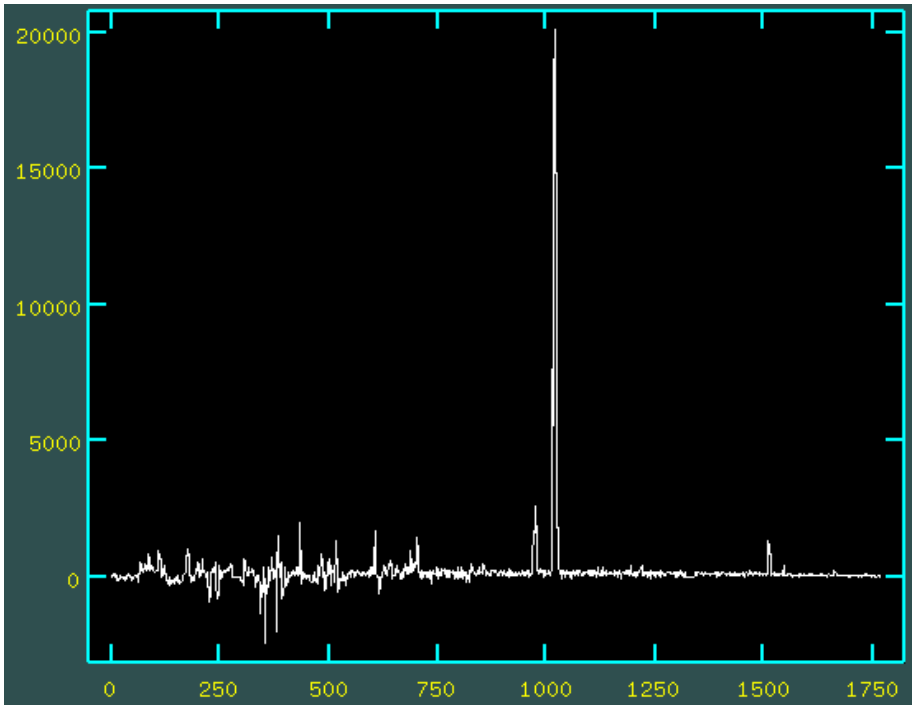

(e) The output spectrum from the APALL routine. The left side is the blue end of the spectrum, and the right side is the red end. The y axis is measured in counts as it has yet to be converted to flux, the x axis is pixels across the length of the slit.

Figure 2.5: The interactive steps steps in APALL to extract a spectrum.

I was calibrating. The REIDENTIFY routine did not produce good results automatically as it is vulnerable to second order contamination so I did this for each spectrum in interactive mode. I then applied the resulting correction to the respective spectra using the DISPCOR routine.

Flux Calibration

To convert my data from counts to flux I used the standard stars EG21 and LTT1020 as comparisons. Given that I didn't use the Gemini IRAF routines to wavelength calibrate and extract my slits, I decided to not use them to flux calibrate either. Instead, I used the NOAO IRAF STANDARD routine to tabulate the standard star values. These values were then input into the SENSFUNC routine which calculates a sensitivity function fitted across the CCD, as shown in Fig 2.6. Parts of the spectrum are very noisy and so were excluded from the final fit by deleting these points in SENSFUNC. Also excluded are the points near the chip gap as these may be artificially small.

2.1.3 Photometry

I undertook a photometric survey of NGC6744 for my Bachelor's research project Sharp (2020) which I will compare to my spectroscopic data. As I will be using the results from this work later, I will describe the process used for clarity.

In addition to the GMOS-S data, VLT/FORS1 HeII narrow band imaging is available for NGC 6744. Narrow band filters centered on HeII λ4686 and Off HeII λ4750 were used to measure the HeII emission and the continuum close to it. The continuum flux is subtracted from HeII flux to find the helium excess, i.e. how much more a source emits in the narrow wavelength range of the HeII narrowband filter than the continuum. This data was reduced using IRAF IMARITH and IMCOMBINE routines with bias and flat field images taken on the observing nights.

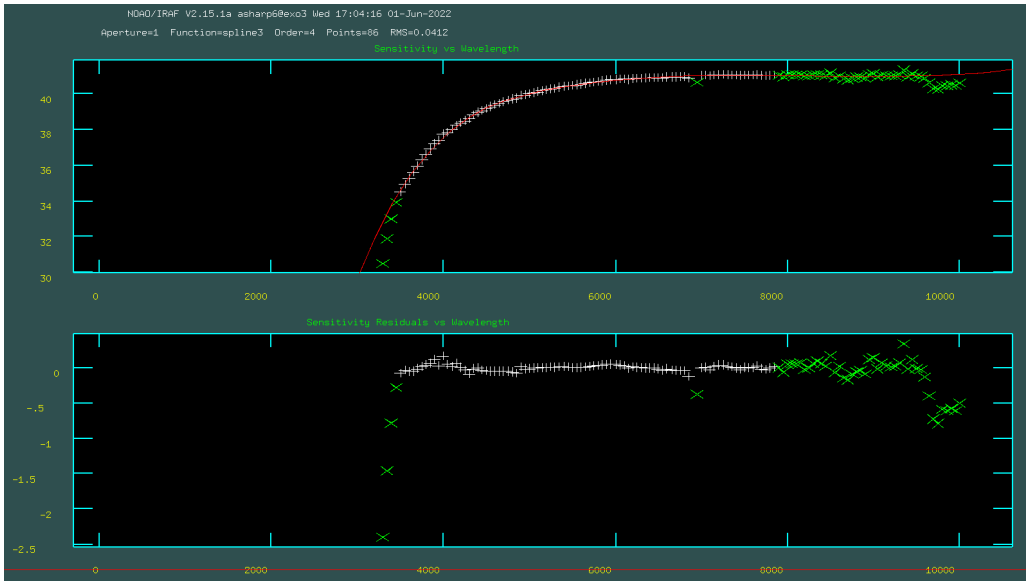

Figure 2.6: This shows the fitting of the sensitivity function. The white crosses are data that is being used in the fit and the green crosses are data that is being excluded from the fit. The red line shows the current fit. The top plot shows the difference between the standard values for the standard star and the measured data values. The bottom plot shows the residuals of each data point from the fit.

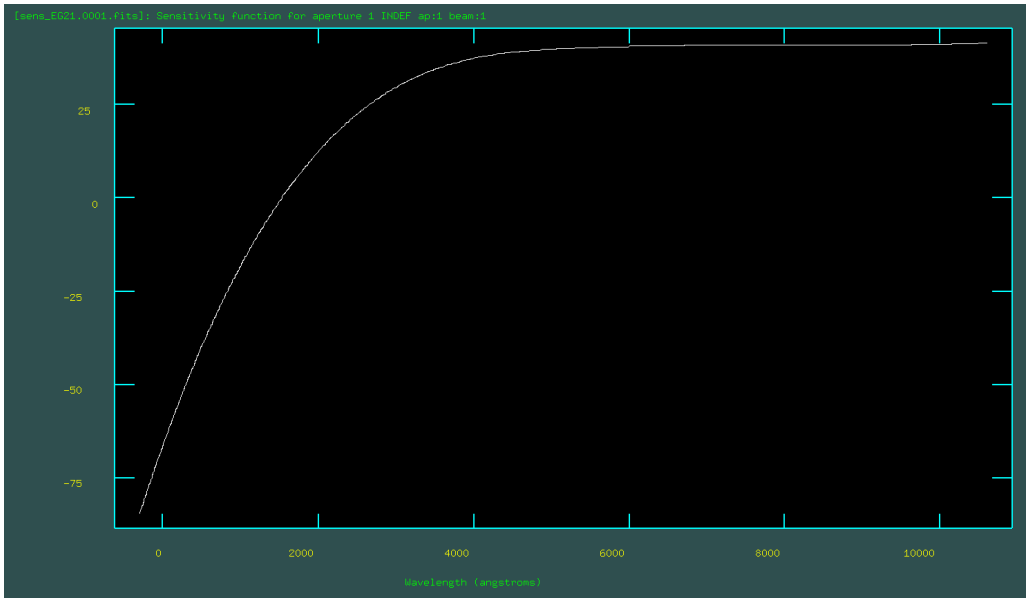

Figure 2.7: The sensitivity function output from SENSFUNC.

The data include standard star fields of the standard star CD 34 241 [2]. The standard star was only observed in the top chip for this data, but a numerical comparison of background values in the top and bottom chips found negligible differences so the zero point calculated for the top chip was used for both.

Using the IRAF DAOPHOT routine I performed crowded field photometry on the reduced VLT FORS1 data. As several of my sources are faint or in very crowded regions finding the correct variables to use required a mixture of data values extracted using IMEXAMINE and trial and error. I first created a point spread function (PSF) for each image. To do this I ran the IRAF DAOPHOT routine PHOT, to find the objects in the image and calculate their magnitudes, then PSTSELECT, to select stars for use in the PSF routine. Foreground stars are unlikely to be point like and are generally brighter than stars within the galaxy, therefore they will skew the resulting PSF. I used the Gaia catalogue overplotted on the HeII image in the Starlink Gaia program to avoid selecting any foreground stars for my PSF stars. Once I was happy with my PSF, I ran the NSTAR and ALLSTAR routines to check that DAOPHOT was detecting all the correct objects. Then, once the ideal variables had been determined, I took the output list from ALLSTAR and ran a Fortran code to merge the two lists and find the differences in magnitude for each object between the two images. The difference in magnitude between these two images measures the helium excess and is used to identify potential WR stars via strong HeII emission.

2.1.4 Spectral Analysis

Line Fitting

I used the Emission Line Fitting (henceforth ELF) commands within the program DIPSO to fit Gaussian functions to my spectra. An example of this is shown in Fig. 2.8. DIPSO then uses the values from the data to calculate the flux from the Gaussian curves. This

[2] In the Hamuy et al (1992 and 1994) catalogues this star is mistakenly identified as LTT377 according to the ESO website.

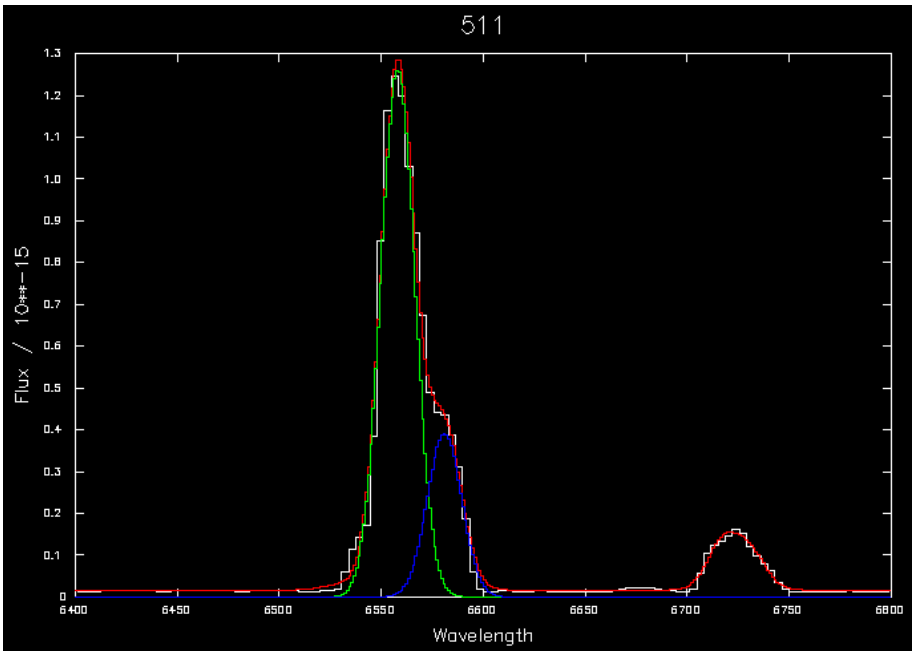

Figure 2.8: This figure shows the Gaussian fits to the unresolved Hα-[NII] emission lines in one of the spectra. The red line shows the overall fit, with green line showing the Hα fit and blue line showing the [NII] fit. To the right is the unresolved [SII] doublet. The [SII] doublet does not have the underlying Gaussian fits visible. The NII 6548λ line is not resolved enough in this spectrum to fit independently.

program calculates a peak flux from the maximum of the curve and a total flux from the area under the curve. Going forward I will refer to total flux simply as flux.

Extinction Correction

Interstellar dust can artificially reduce the flux measured from objects, especially those found in other galaxies. Therefore, the amount of flux reduced, also known as extinction, must be calculated and a correction applied to the data to remove its effects.

I used Balmer line $\frac{H\alpha}{H\beta}$ ratios to calculate the extinction correction for my spectra. The corrections were calculated for each region using the following equation from Conti et al. (2008).

$$\frac{F(H\alpha)}{F(H\beta)} = \frac{I(H\alpha)}{I(H\beta)} 10^{-c(H\beta)[x(H\alpha)-x(H\beta)]} \tag{2.1}$$

I assumed a standard Cardelli et al., 1989 $R_V = 3.1$ extinction law where $x(H\alpha) - x(H\beta) = -0.346$ and an intrinsic ratio $\frac{I(H\alpha)}{I(H\beta)} = 2.86$. I then rearranged the following equation to fit into Equation 2.1

$$E(B-V) \approx 0.77c(H\beta) \tag{2.2}$$

And then rearranged further to make E(B-V) the subject. This results in the following equation:

$$E(B-V) = \left(-\frac{0.77}{0.346}\right) log\left(2.86\frac{F(H\beta)}{F(H\alpha)}\right) \tag{2.3}$$

The extinction correction was then applied to the spectrum using the DIPSO function DRED.

Four of the spectra had Balmer line ratios which yielded negative extinction corrections. In these cases the correction was set to 0.

Template Fitting

In order to identify which subclass each WR star belongs to, it must be compared to previously known WR stars. To do this, templates are made for each subclass. These WR template spectra are created by averaging a sample of known WR stars. I used templates made by Professor Paul Crowther (Crowther et al., 2023) created from Galactic WR stars. I chose these templates due to NGC6744's high metallicity, which is closer to Galactic metallicity than the metallicity in the Large or Small Magellanic Clouds, the other available templates.

The observed spectra are plotted with the template spectra to compare spectral features by eye. In some cases, multiple templates must be combined to form the features shown in the data. In this case, the spectrum is considered to have come from a cluster containing

both these subtypes of WR star. Where the template flux had to be multiplied in order to fit to the data, the source was considered to contain multiple stars of that template's equivalent subtype equal to the value of multiplication. So if a template had to multiply the flux values by 3 to match the data, that source was considered to contain 3 stars. The WC stars are differentiated from WN stars by the presence of a carbon emission line around λ5808Å.

Metallicity

Once the spectrum is extinction corrected, the corrected fluxes can be fitted using ELF and used to calculate the metallicity of the region. None of the slits had a well resolved weak [OIII] λ 4363 lines therefore I used the following O3N2 and N2 relation equations from Marino et al. (2013) adapted from those in Pettini & Pagel (2004).

$$12 + log(O/H) = 8.533[\pm 0.012] - 0.214[\pm 0.012] \times O3N2 \tag{2.4}$$

where O3N2 is given by

$$O3N2 = log\left(\frac{[OIII]\lambda 5007}{H\beta} \times \frac{H\alpha}{[NII]\lambda 6583}\right) \tag{2.5}$$

and

$$12 + Log(O/H) = 8.743[\pm 0.027] - 0.462[\pm 0.024] \times N2 \tag{2.6}$$

where N2 is given by

$$N2 = log\left(\frac{[NII]\lambda 6583}{H\alpha}\right) \tag{2.7}$$

Not all of the spectra displayed [OIII] λ 5007 emission lines which prevented the use of the O3N2 relation to calculate metallicity for these regions. Likewise, not all the spectra displayed [NII] λ 6583 lines, however, those spectra that did not display [NII] lines either did not display enough features to approximate the extinction or were not emission line spectra.

2.1.5 Deprojected Radius

To further investigate the properties of NGC6744 the deprojected galactocentric distance to each source was calculated using a Fortran script written by Dr P. Massey and then adapted by Prof. P. Crowther and myself (private communication). This code calculates the distance of the source from the centre of the galaxy as a ratio of the radius at which the source is found divided by the R_{25} distance, which is the distance at which the magnitude of the galaxy disc drops to 25 magnitudes/arcsecond^2 in the B band.

As NGC6744 is not perfectly face on to the observer, the inclination and position angle (see Table 1.1) of the galaxy must be used to find the direct line between the centre of the galaxy and each object. Then, the distance between the two can be calculated. Dividing by the R_{25} distance then shows the ratio of the radius this distance is, which can be used to calculate gradients across the galaxy.

Once the distance from the center of NGC6744 is calculated, this value was plotted against the metallicity of the sources to find the gradient of metallicity across the galaxy. In addition, I plotted number of WR stars against radius, to show where in the galaxy they are found. To increase the number of WR stars in this plot, I included the list of WR candidates I found during my Bachelors project (see Appendix A) (Sharp, 2020).

Chapter 3

Results

Of the 25 slits in Mask 5, 4 had multiple objects that could be extracted from the slit, of which one slit contained 3 objects. Therefore, the number of spectra extracted from Mask 5 was 30 in total. However, of the 30 spectra extracted, only 19 had the diagnostic Balmer hydrogen lines used to calculate extinction corrections and metallicities.

Of the 11 spectra without usable hydrogen lines, 3 spectra had absorption spectra characteristic of O or B type stars and 4 lacked any kind of stellar features or nebular lines. The slits without nebular lines can be explained by the fact that some slits were placed to fill out the mask and not over a HeII source. Both the non-HII region spectra and the non-WR star spectra were excluded from the metallicity calculations and WR template matching as the methods I used are not usable in these cases.

For 5 of the usable slits the calculations for the extinction correction had a negative result. Given that negative extinction is unphysical, it is likely that underlying $H\beta$ absorption has affected an already low $H\beta$ flux. In these cases, I set the extinction correction to 0. In Table 3.1 these slits are denoted by an * in the E(B-V) column. The fluxes on these slits are artificially smaller than the others because of the lack of extinction correction and so any properties derived from them are also be artificially reduced compared to those of the other slits.

For both the imaging data and the MOS masks, the observation FoV did not cover the

whole galaxy. NGC 6744 has an optical FoV of $20'x13'$ (Yew et al., 2018) and cannot be fit entirely in the FoV of either the Gemini South MOS instrument or the VLT FORS1 instrument. While there were 3 masks worth of slits available, I only extracted one. In addition, the Gemini-South FoV is only $5.5'x5.5'$. Therefore completeness can only be considered within this sample. This will be discussed in more detail in Section 4.

3.1 Fluxes

Nineteen of the extracted spectra had Hα and Hβ lines that could be fitted. Sixteen of these spectra had both [NII] and [OIII] lines while 3 had only [NII] lines and no [OIII]. These lines will be discussed further in Section 3.3.

Table 3.1: Table of $H\alpha$ and $H\beta$ fluxes without extinction correction applied. These hydrogen fluxes were used to calculate an extinction correction, given in the E(B-V) column. * These extinction corrections were set to 0 as the output of the calculation was originally negative.

ID	RA	Dec	Hα flux	error	Hβ flux	error	E(B-V)	error
MO5 S1	19:10:02	-63:54:37.55	1.96E-15	9.00E-17	7.1E-16	1.8E-16	0.00 *	0.20
MO5 S2	19:10:07	-63:54:47.92	2.06E-16	7.00E-18	2.8E-16	5.0E-17	0.00 *	0.17
MO5 S3	19:09:42	-63:53:47.11	-	-	-	-	-	-
MO5 S4	19:09:49	-63:53:57.37	-	-	-	-	-	-
MO5 S5	19:09:56	-63:54:16.64	8.35E-16	1.60E-17	3.6E-16	4.0E-17	0.00 *	2.00
MO5 S6	19:09:36	-63:54:06.05	1.89E-14	2.00E-16	2.69E-15	6.00E-17	0.87	0.02
MO5 S7	19:09:43	-63:54:29.85	2.646E-14	1.500E-16	8.30E-15	1.30E-16	0.10	0.02
MO5 S8	19:09:35	-63:53:29.61	9.66E-15	7.00E-17	3.32E-15	7.00E-17	0.02	0.02
MO5 S9	19:09:57	-63:53:17.74	-	-	-	-	-	-
MO5 S10	19:10:03	-63:53:11.29	4.74E-15	4.00E-17	4.7E-16	3.0E-17	1.21	0.06
MO5 S11	19:09:58	-63:52:51.60	-	-	-	-	-	-
MO5 S12	19:10:08	-63:52:28.60	-	-	-	-	-	-

Continued on next page

Table of $H\alpha$ and $H\beta$ fluxes without extinction correction applied. These hydrogen fluxes were used to calculate an extinction correction, given in the E(B-V) column. * These extinction corrections were set to 0 as the output of the calculation was originally negative.

ID	RA	Dec	Hα flux	error	Hβ flux	error	E(B-V)	error
MO5 S13	19:10:15	-63:52:34.61	-	-	-	-	-	-
MO5 S14 - 1	19:09:58	-63:52:57.15	3.29E-16	4.00E-18	1.13E-16	9.00E-18	0.02	0.08
MO5 S14 - 2	19:09:58	-63:52:57.15	-	-	-	-	-	-
MO5 S14 - 3	19:09:58	-63:52:57.15	1.077E-15	7.000E-18	1.62E-16	1.00E-17	0.81	0.06
MO5 S15	19:10:10	-63:52:44.94	-	-	-	-	-	-
MO5 S16	19:10:11	-63:51:44.64	1.05E-14	2.00E-16	2.05E-15	1.60E-16	0.56	0.08
MO5 S17 - 1	19:10:12	-63:52:01.23	1.305E-14	1.400E-16	3.36E-15	3.00E-17	0.30	0.013
MO5 S17 - 2	19:10:12	-63:52:01.23	-	-	-	-	-	-
MO5 S18	19:10:04	-63:51:01.59	6.18E-15	1.00E-16	9.9E-16	3.0E-17	0.76	0.04
MO5 S19 - 1	19:09:35	-63:51:13.40	3.055E-15	1.800E-17	5.11E-16	1.20E-17	0.71	0.02
MO5 S19 - 2	19:09:35	-63:51:13.40	9.6E-16	7.0E-17	2.4E-16	2.0E-17	0.31	0.12
MO5 S20	19:09:55	-63:51:23.66	2.285E-14	1.800E-16	4.3E-15	1.0E-16	0.61	0.02

Continued on next page

Table of $H\alpha$ and $H\beta$ fluxes without extinction correction applied. These hydrogen fluxes were used to calculate an extinction correction, given in the E(B-V) column. * These extinction corrections were set to 0 as the output of the calculation was originally negative.

ID	RA	Dec	Hα flux	error	Hβ flux	error	E(B-V)	error
MO5 S21	19:10:09	-63:51:36.40	1.242E-14	6.000E-17	3.16E-15	6.00E-17	0.31	0.02
MO5 S22	19:10:01	-63:49:50.92	2.19E-15	3.00E-17	1.24E-15	3.00E-17	0.00 *	0.03
MO5 S23	19:10:10	-63:49:58.29	-	-	-	-	-	-
MO5 S24	19:10:05	-63:50:16.72	6.67E-14	5.00E-16	1.01E-14	1.60E-16	0.81	0.02
MO5 S25 - 1	19:09:58	-63:50:35.77	-	-	-	-	-	-
MO5 S25 - 2	19:09:58	-63:50:35.77	3.69E-14	3.00E-16	1.323E-14	9.000E-17	0.00 *	0.01

Table 3.2: Table of fluxes with extinction corrections applied.

ID	RA	Dec	Hα flux	Hβ flux	O3(5007Å) flux	N2(6583Å) flux	Metallicity (N2)	error	Metallicity (O3N2)	error
MO5 S1	19:10:02	-63:54:37.55	1.91E-15	7E-16	-	8.5E-16	8.580	0.007	-	-
MO5 S2	19:10:07	-63:54:47.92	2.06E-16	2.8E-16	8.9E-16	4.2E-17	8.42	0.03	8.25	0.02
MO5 S3	19:09:42	-63:53:47.11	-	-	-	-	-	-	-	-
MO5 S4	19:09:49	-63:53:57.37	-	-	-	-	-	-	-	-
MO5 S5	19:09:56	-63:54:16.64	8.1E-16	3.6E-16	9E-17	4.01E-16	8.603	0.008	8.67	0.04
MO5 S6	19:09:36	-63:54:06.05	1.35E-13	5.10E-14	7.5E-15	2.03E-14	8.362	0.009	8.63	0.02
MO5 S7	19:09:43	-63:54:29.85	3.29E-14	1.09E-14	1.5E-15	1.06E-14	8.515	0.005	8.71	0.02
MO5 S8	19:09:35	-63:53:29.61	9.27E-15	3.51E-15	4.36E-15	6.08E-15	8.658	0.003	8.564	0.003
MO5 S9	19:09:57	-63:53:17.74	-	-	-	-	-	-	-	-
MO5 S10	19:10:03	-63:53:11.29	4.6E-14	2.60E-14	1.7E-14	1.24E-14	8.479	0.013	8.51	0.03
MO5 S11	19:09:58	-63:52:51.60	-	-	-	-	-	-	-	-
MO5 S12	19:10:08	-63:52:28.60	-	-	-	-	-	-	-	-
MO5 S13	19:10:15	-63:52:34.61	-	-	-	-	-	-	-	-

Continued on next page

Table of fluxes with extinction corrections applied.

ID	RA	Dec	Hα flux	Hβ flux	O3(5007Å) flux	N2(6583Å) flux	Metallicity (N2)	error	Metallicity (O3N2)	error
MO5 S14 - 1	19:09:58	-63:52:57.15	3.45E-16	1.12E-16	5E-18	2.25E-16	8.658	0.006	8.89	0.08
MO5 S14 - 2	19:09:58	-63:52:57.15	-	-	-	-	-	-	-	-
MO5 S14 - 3	19:09:58	-63:52:57.15	5.83E-15	2.47E-15	4.6E-16	1.19E-15	8.425	0.005	8.62	0.02
MO5 S15	19:10:10	-63:52:44.94	-	-	-	-	-	-	-	-
MO5 S16	19:10:11	-63:51:44.64	2.84E-14	1.46E-14	-	1.04E-14	8.541	0.008	-	-
MO5 S17 - 1	19:10:12	-63:52:01.23	2.61E-14	9.85E-15	5.46E-15	6.8E-15	8.472	0.007	8.553	0.004
MO5 S17 - 2	19:10:12	-63:52:01.23	-	-	-	-	-	-	-	-
MO5 S18	19:10:04	-63:51:01.59	3.50E-14	1.23E-14	3.0E-15	3.6E-15	8.284	0.015	8.55	0.04
MO5 S19 - 1	19:09:35	-63:51:13.40	1.553E-14	5.57E-15	3.0E-16	2.65E-15	8.388	0.007	8.74	0.02
MO5 S19 - 2	19:09:35	-63:51:13.40	2.19E-15	7.7E-16	3.8E-16	8.7E-16	8.557	0.007	8.61	0.02
MO5 S20	19:09:55	-63:51:23.66	8.99E-14	3.42E-14	3.1E-15	1.21E-14	8.341	0.014	8.66	0.02
MO5 S21	19:10:09	-63:51:36.40	2.16E-14	7.294E-15	5.9E-16	6.38E-15	8.498	0.005	8.75	0.02
MO5 S22	19:10:01	-63:49:50.92	2.19E-15	1.24E-15	-	1.45E-15	8.660	0.007	-	-

Continued on next page

Table of fluxes with extinction corrections applied.

ID	RA	Dec	Hα flux	Hβ flux	O3(5007Å) flux	N2(6583Å) flux	Metallicity (N2)	error	Metallicity (O3N2)	error
MO5 S23	19:10:10	-63:49:58.29	-	-	-	-	-	-	-	-
MO5 S24	19:10:05	-63:50:16.72	3.95E-13	1.51E-13	8.0E-14	1.60E-13	8.562	0.007	8.597	0.009
MO5 S25 - 1	19:09:58	-63:50:35.77	-	-	-	-	-	-	-	-
MO5 S25 - 2	19:09:58	-63:50:35.77	3.76E-14	1.338E-14	2.36E-15	1.29E-14	8.528	0.004	8.691	0.004

3.2 WR stars

Overall in Mask 05, I found 17 WC stars and 18 WN stars across 7 WR regions. There is not enough variety within these groups to perform a granular analysis of position and metallicity for the numerical subclasses, therefore I will analyse them more generally based on the categories WN and WC.

In addition to these stars, 3 of the slits had chip gaps over one or more diagnostic lines which prevented a clear identification of potential WR features. These stars have not been given a WR subtype as the HeII bumps were not able to be fitted. Two of the sources had very high continuum levels, which prevented fitting of Galactic templates to the WR features. These 2 sources are likely large clusters, which is discussed more in Section 4.2.

Extrapolating from the sources found in this mask, if the number of WR stars is the same in each mask then I would expect $\sim$ 105 WR stars in $\sim$ 20 sources in total from all three masks combined. As I was unable to extract magnitudes for all of the confirmed WR stars, I am unable to extrapolate which of my photometric WR candidates are also WR stars.

The 18 WN stars were all found in groups containing both WN stars and WC stars. No spectra were found to contain only WN stars. Five of the sources that contained WC stars also contained WN stars(Fig. 3.2, 3.5, 3.6, 3.7) and 2 of the sources contained only WC stars(Fig. 3.1, 3.4). All of the sources that contained only WC stars appeared to be in groups or clusters.

3.3 Metallicity

The metallicities were calculated using the two relations described in Section 2.1.4. They were calculated for each slit for which Hα, Hβ, [NII] 6583λ and [OIII] 5007λ fluxes were found. For those slits without [OIII] 5007λ fluxes, only the N2 metallicity was calculated. Therefore, the plot of N2 metallicities has 19 points and the plot of O3N2 metallicity has

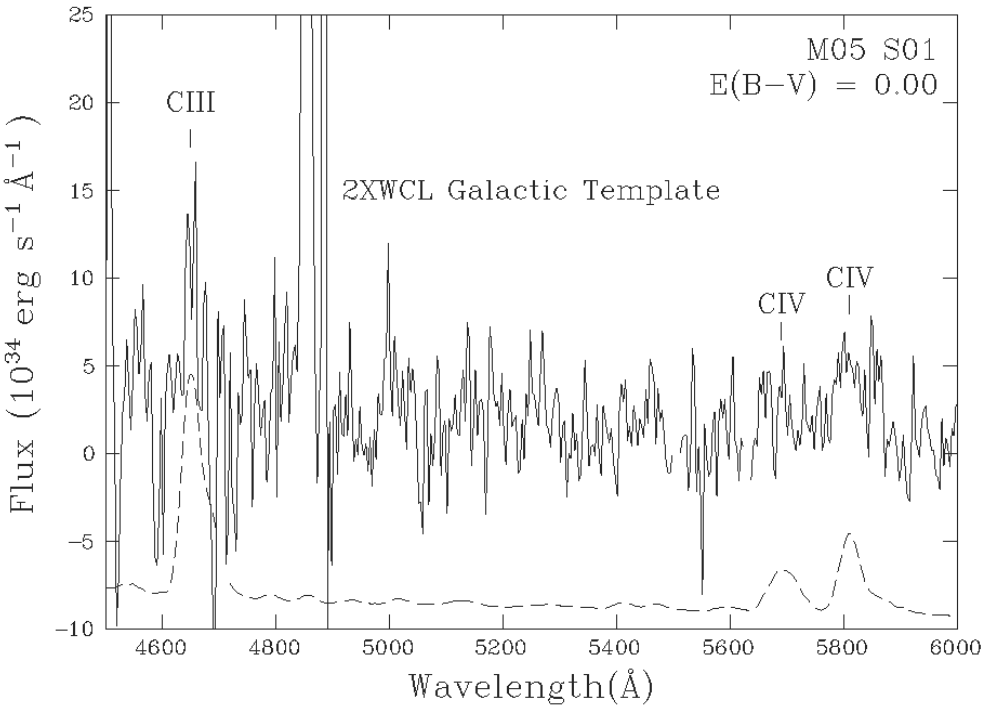

Figure 3.1: Plot of the spectrum extracted from M05 1 with the WCL template overplotted. The template flux was multiplied by 2 to fit the flux of the data. The carbon emission lines are highlighted. The WC template is plotted with a dashed line and the data with a solid line.

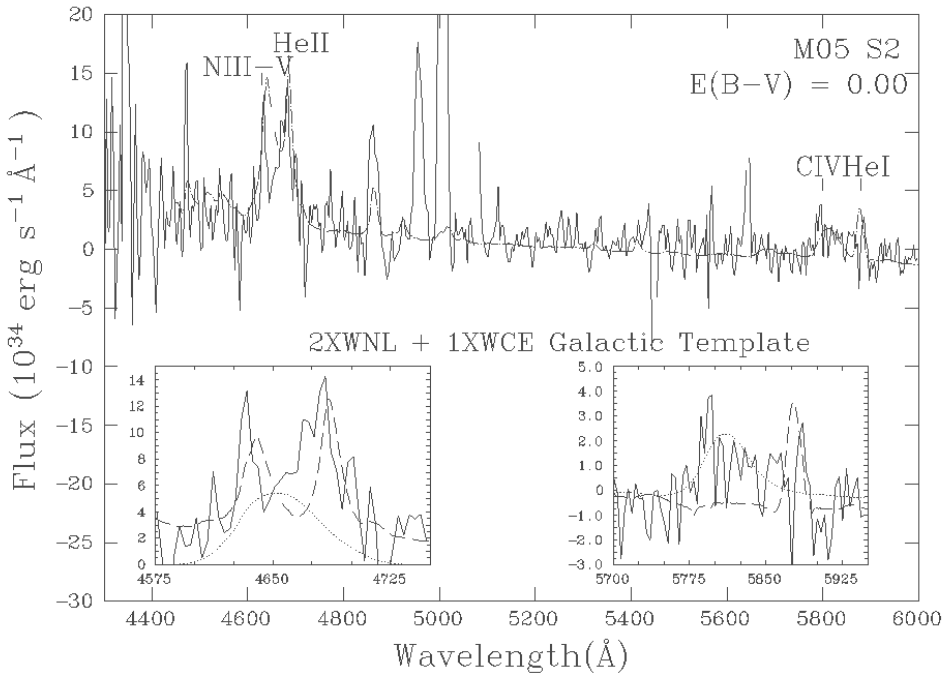

Figure 3.2: Plot of the spectrum extracted from M05 2 with the WNL and WCE templates overplotted. The flux of the WN template was multiplied by 2 to fit the flux of the data, particularly the NII emission line. The WC template is plotted with a dashed line; the WN template with a dotted line; the combined templates with a dot dash line; and the data with a solid line. The carbon, nitrogen and helium emission lines are labelled.

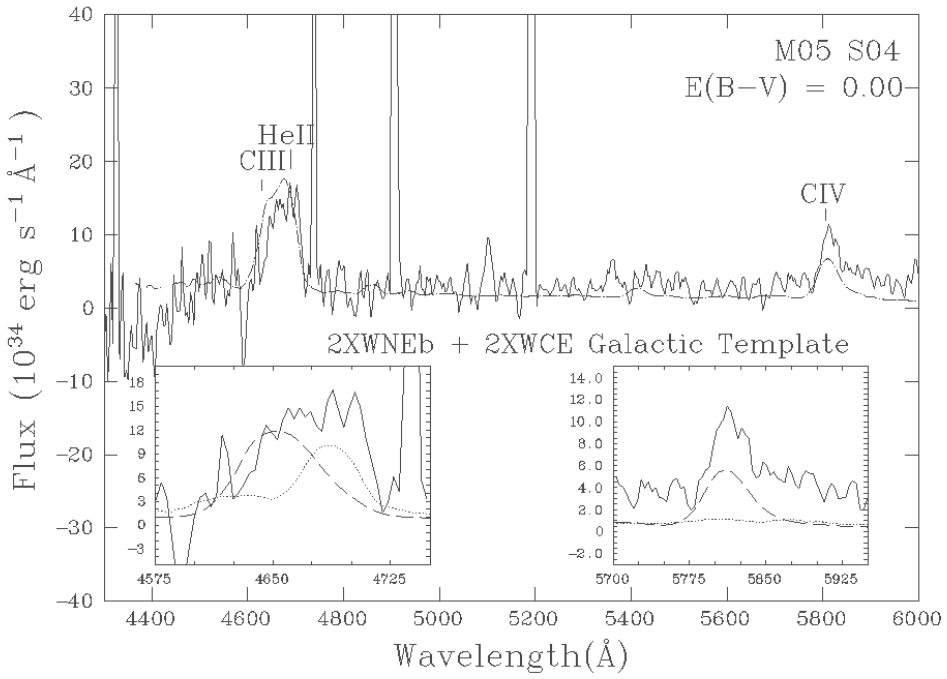

Figure 3.3: Plot of the spectrum extracted from M05 4 with the WNL and WCE templates overplotted. Both the WN and WC template fluxes were multiplied by 2 to fit the flux of the data. The WC template is plotted with a dashed line; the WN template with a dotted line; the combined templates with a dot dash line; and the data with a solid line. The carbon and helium emission lines are labelled.

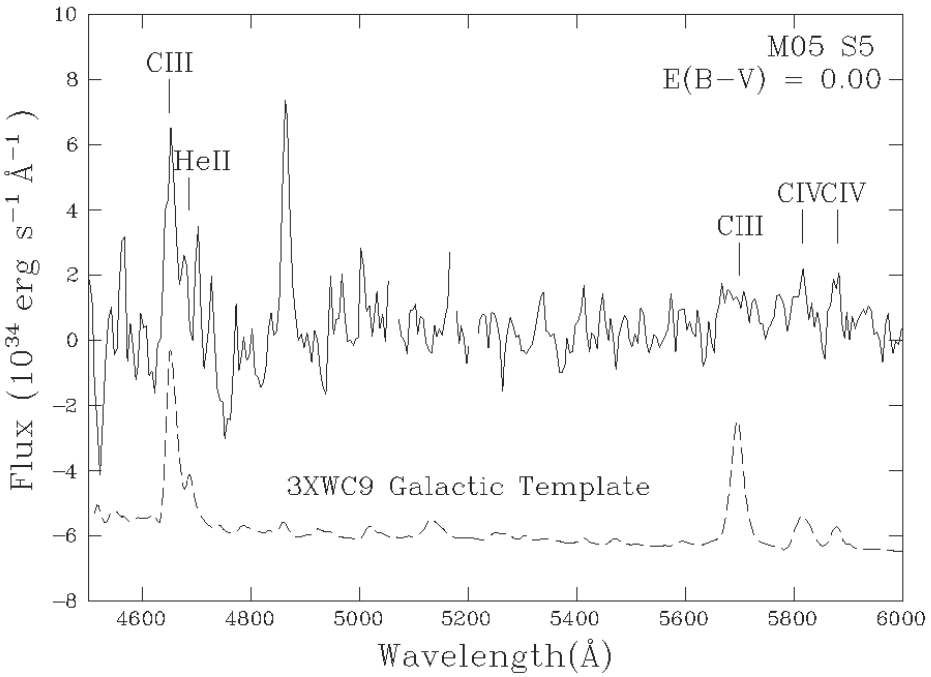

Figure 3.4: Plot of the spectrum extracted from M05 5 with the WC9 template overplotted at an offset. The WC template flux was multiplied by 3 to fit the data flux. The WC template is plotted with a dashed line and the data with a solid line. The carbon and helium emission lines are labelled.

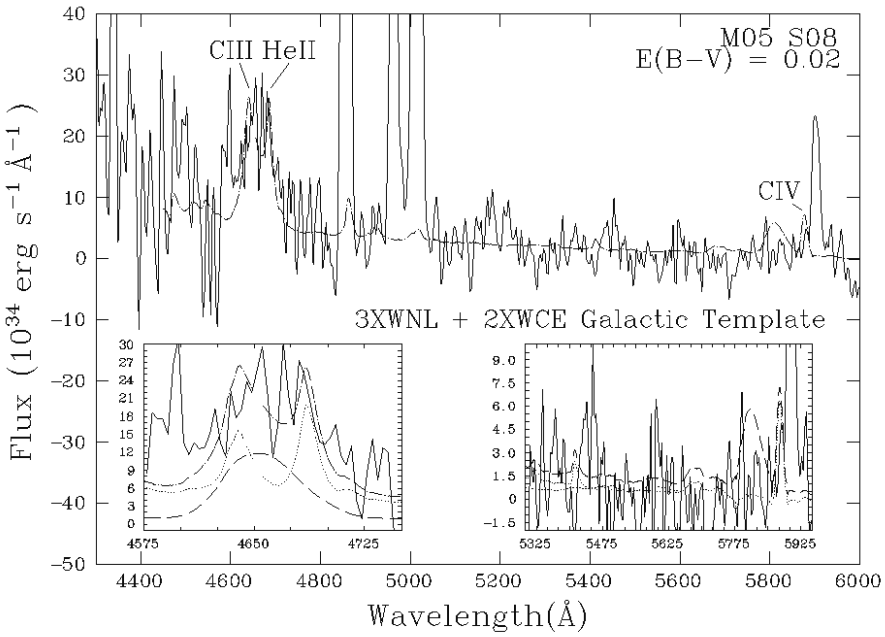

Figure 3.5: Plot of the spectrum extracted from M05 8 with WNL and WCE templates overplotted. The flux of the WN template is multiplied by 3 and the flux of the WC template is multiplied by 2 to match the flux of the data. The WC template is plotted with a dashed line; the WN template with a dotted line; the combined templates with a dot dash line; and the data with a solid line. The carbon and helium emission lines are labelled.

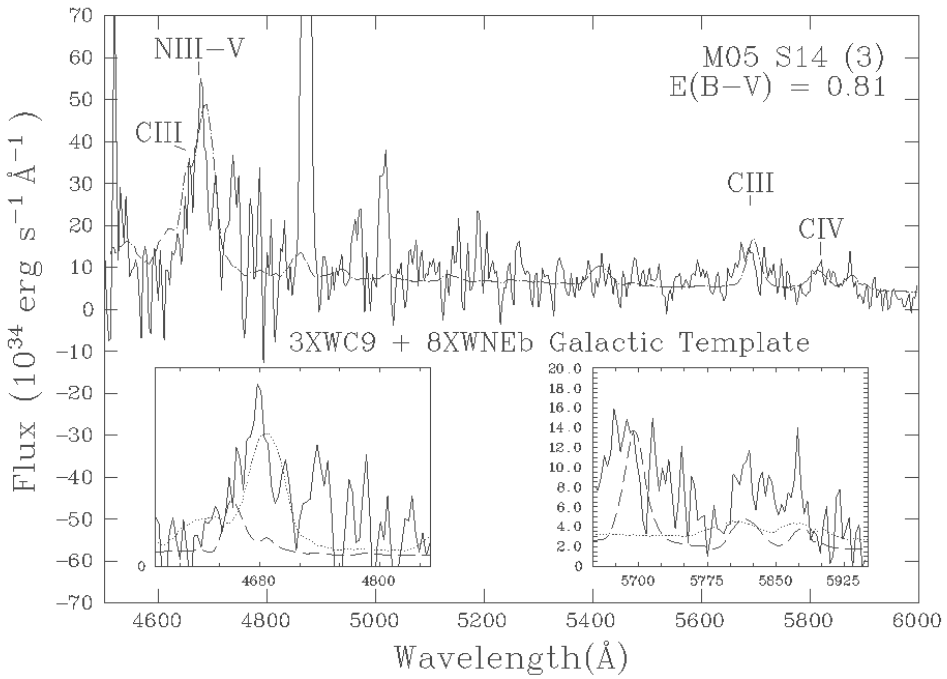

Figure 3.6: Plot of the spectrum extracted from M05 14-3 with the WC9 and WNEb templates overplotted. The flux of the WN template is multiplied by 8 and the flux of the WC template is multiplied by 3 to match the flux of the data. The WC template is plotted with a dashed line; the WN template with a dotted line; the combined templates with a dot dash line; and the data with a solid line. The carbon and nitrogen emission lines are labelled.

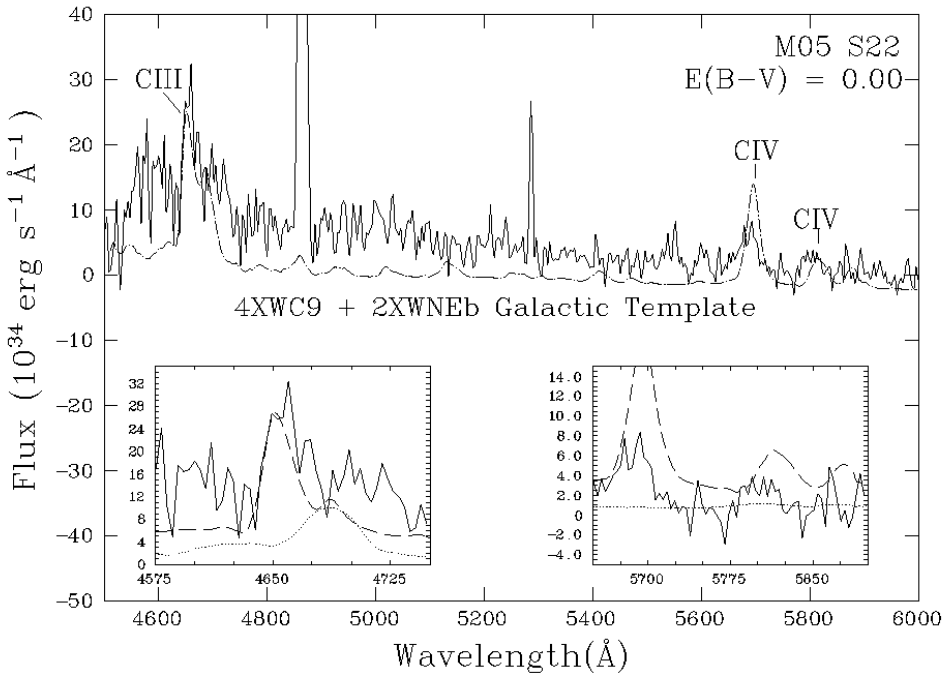

Figure 3.7: Plot of the spectrum extracted from M05 22 with the WC9 and WNEb templates overplotted. The WN template flux is multiplied by 2 and the WC template flux is multiplied by 4 to match the flux of the data. The WC template is plotted with a dashed line; the WN template with a dotted line; the combined templates with a dot dash line; and the data with a solid line. The carbon emission lines are labelled.

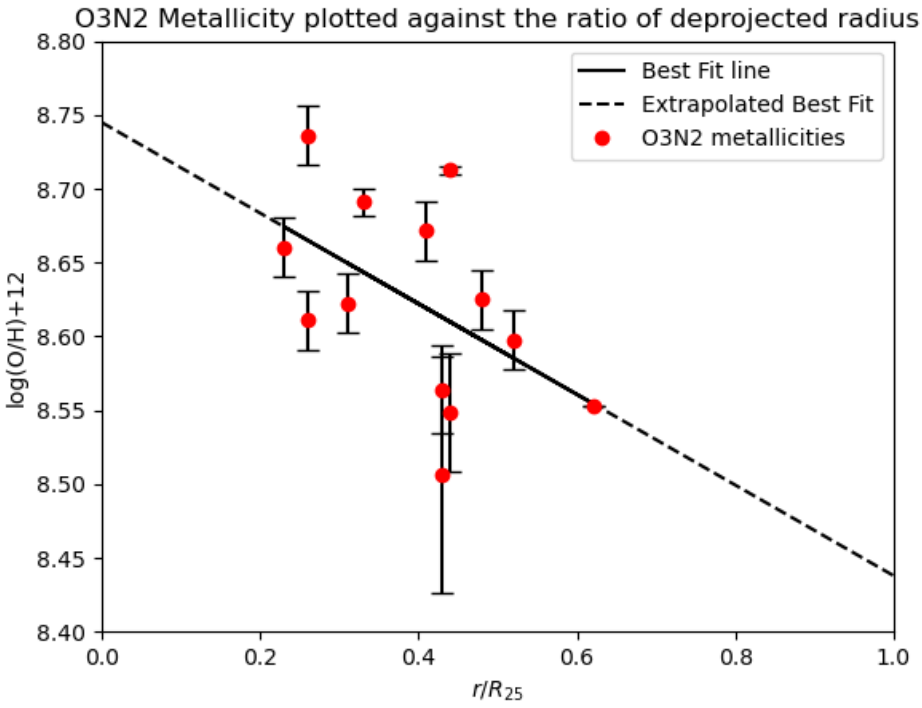

Figure 3.8: Scatterplot of the metallicities derived using the O3N2 relation with a line of best fit. The best fit line has been extrapolated across the whole radius range. Spectra which had their extinction correction set to 0 have been removed from the plot.

16.

The group of spectra where the extinction correction was set to 0 have artificially low N2 metallicities, so these 5 objects were removed from the dataset when calculating metallicity gradients.

The N2 metallicity gradient is Log O/H + 12 = $(8.70 \pm 0.07) - (0.32 \pm 0.11)\frac{r}{R_{25}}$. The O3N2 metallicity gradient is Log O/H + 12 = $(8.74 \pm 0.07) - (0.31 \pm 0.11)\frac{r}{R_{25}}$. As can be seen in Fig.3.10, O3N2 has a shallower gradient but a larger intercept compared to N2. However, both data sets overlap.

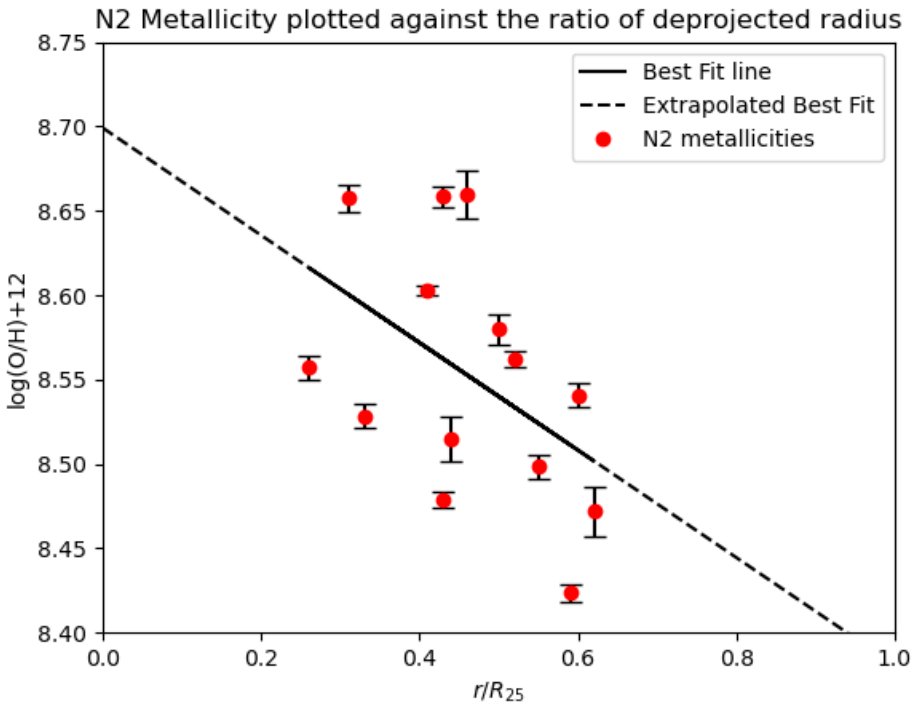

Figure 3.9: Scatterplot of the metallicities derived using the N2 relation with a line of best fit. The best fit line has been extrapolated across the whole radius range. Spectra which had their extinction correction set to 0 have been removed.

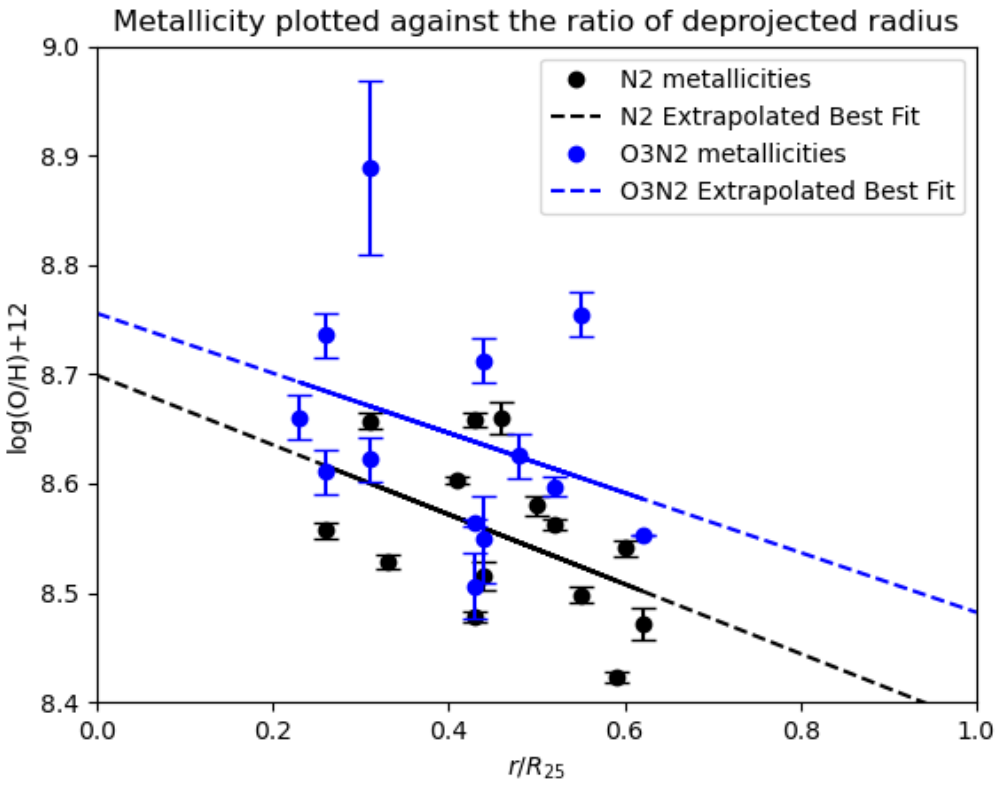

Figure 3.10: The O3N2 and N2 metallicity scatterplots and best fit lines plotted on the same graph. This shows an offset between best fit lines and an overlap in metallicity range. The best fit lines have been extrapolated across the whole radius range. Spectra which had their extinction correction set to 0 have been removed.

3.4 HeII Magnitudes

During my Bachelors degree I undertook a survey of photometric WR candidates using narrow band imaging centered on 4686Å (Sharp, 2020). Shown in Table 3.3 are the magnitudes from this catalogue that correspond to objects in Mask 05. I attempted to repeat this process with different variables, such as minimum size of object and full width half maximum, in order to measure magnitudes for all of the slits. However, none of these changes managed to calculate magnitudes for a greater number of target objects. Unfortunately, this means that only 13 of the spectra have HeII magnitudes recorded. Several of the candidates were in very crowded regions which prevented accurate measurements. In addition, many of the targets in this mask are very faint which may have prevented their magnitudes being calculated. Overall, this meant that half the sources do not have HeII magnitudes available and only 3 WR sources have HeII excesses.

Table 3.3: Table of HeII magnitudes.

ID	RA	Dec	HeII mag	HeII excess
M05 S1	19:10:02	-63:54:37.55	-	-
M05 S2	19:10:07	-63:54:47.92	-	-
MO5 S3	19:09:42	-63:53:47.11	22.97	1.29
MO5 S4	19:09:49	-63:53:57.37	22.78	0.78
MO5 S5	19:09:56	-63:54:16.64	23.35	1.04
MO5 S6	19:09:36	-63:54:06.05	-	-
MO5 S7	19:09:43	-63:54:29.85	22.32	0.01
MO5 S8	19:09:35	-63:53:29.61	22.9	0.63
MO5 S9	19:09:57	-63:53:17.74	-	-

Continued on next page

Table 3.3 – continued from previous page

ID	RA	Dec	HeII mag	HeII excess
MO5 S10	19:10:03	-63:53:11.29	22.88	1.7
MO5 S11	19:09:58	-63:52:51.60	-	-
MO5 S12	19:10:08	-63:52:28.60	-	-
MO5 S13	19:10:15	-63:52:34.61	23.55	0.76
MO5 S14 - 1	19:09:58	-63:52:57.15	-	-
MO5 S14 - 2	19:09:58	-63:52:57.15	-	-
MO5 S14 - 3	19:09:58	-63:52:57.15	-	-
MO5 S15	19:10:10	-63:52:44.94	22.79	0.64
MO5 S16	19:10:11	-63:51:44.64	23.09	0.63
MO5 S17 - 1	19:10:12	-63:52:01.23	-	-
MO5 S17 - 2	19:10:12	-63:52:01.23	-	-
MO5 S18	19:10:04	-63:51:01.59	-	-
MO5 S19 - 1	19:09:35	-63:51:13.40	-	-
MO5 S19 - 2	19:09:35	-63:51:13.40	-	-
MO5 S20	19:09:55	-63:51:23.66	-	-
MO5 S21	19:10:09	-63:51:36.40	-	-
MO5 S22	19:10:01	-63:49:50.92	23.58	-0.12
MO5 S23	19:10:10	-63:49:58.29	-	-
MO5 S24	19:10:05	-63:50:16.72	19.78	0.22
MO5 S25 - 1	19:09:58	-63:50:35.77	21.15	0.93
MO5 S25 - 2	19:09:58	-63:50:35.77	21.15	0.93

Chapter 4

Discussion

4.1 WR Population

The spatial resolution of the GMOS data is 55pc for the 510nm central wavelength and 58pc for the 530nm central wavelength. The spatial resolution is calculated using the angular distance formula. The spatial resolution for the VLT FORS1 data is 50pc. While Giant HII regions have typical diameters of order 100pc, the star cluster at the center of 30 Doradus (for example) is 40pc in diameter (Walborn, 1991) which would result in all 28 known WR stars within the cluster (Neugent et al., 2018) to be observed as 1 object. At the spatial resolutions of my GMOS data, the number of WR stars in this cluster would likely be underestimated and the properties of individual WR stars lost.

Additionally, the luminosity of the WR stars measured in this work is inflated and the emission line strengths diluted by the surrounding stellar population because of the poor spatial resolution. The majority of the WR stars found are in regions which also contain other stars so the spectra of the WR stars are contaminated by them.

In Pledger et al. (2021), the authors show that at spatial resolutions $>$ 40pc less than 40 percent of WR stars will be detected and large clusters will be detected as single blended objects. Knowing then that likely less than 40 percent of WR stars in NGC6744 are visible, it is of interest to see the completeness level of detected stars in general. In Figure

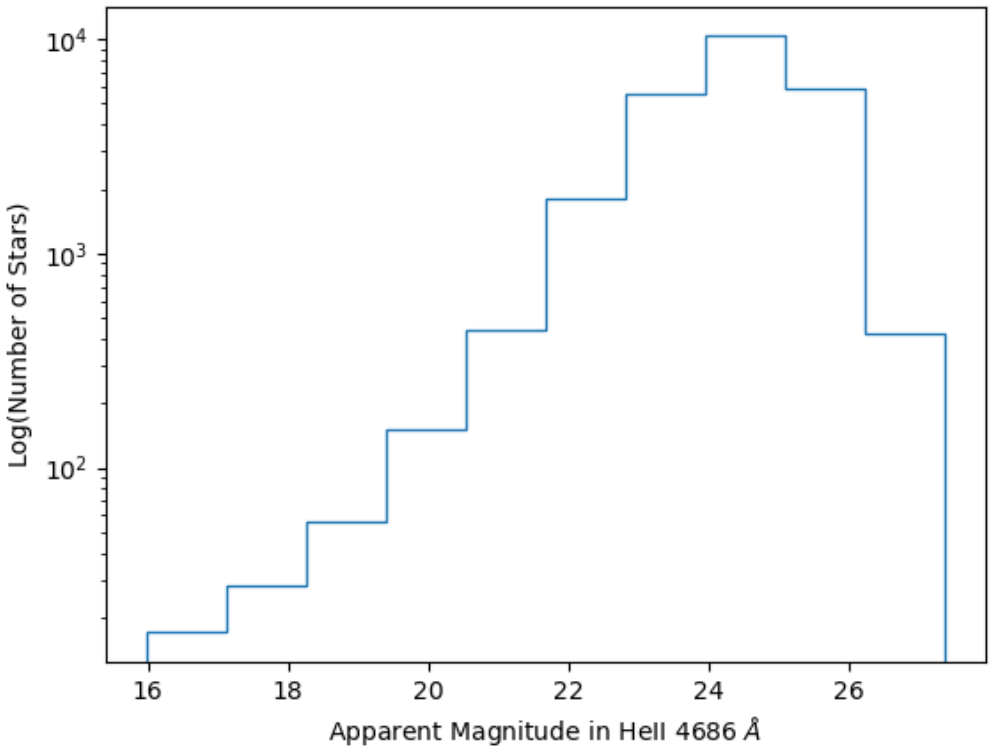

Figure 4.1: A plot of number of stars against HeII 4686Å aparrent magnitude. You can see from the peak of the histogram that the completeness limit is approximately 24mag (Sharp, 2020).

4.1 100 percent detection completeness is found at around 24mag. Any star fainter than this magnitude has a decreasing likelihood of being detected. Converted to absolute magnitude, this lower limit to detection is $\sim -6.86 M_{HeII}$. Typical absolute magnitudes for resolved WR stars range from $-3 M_V$ to $-6 M_V$ and broadband measurements of WR stars tend to overestimate the continuum magnitude by $\sim$ 0.5mag (Crowther, 2007). This would suggest a typical absolute magnitude of $\sim -2.5 M_{HeII}$ to $-5.5 M_{HeII}$.

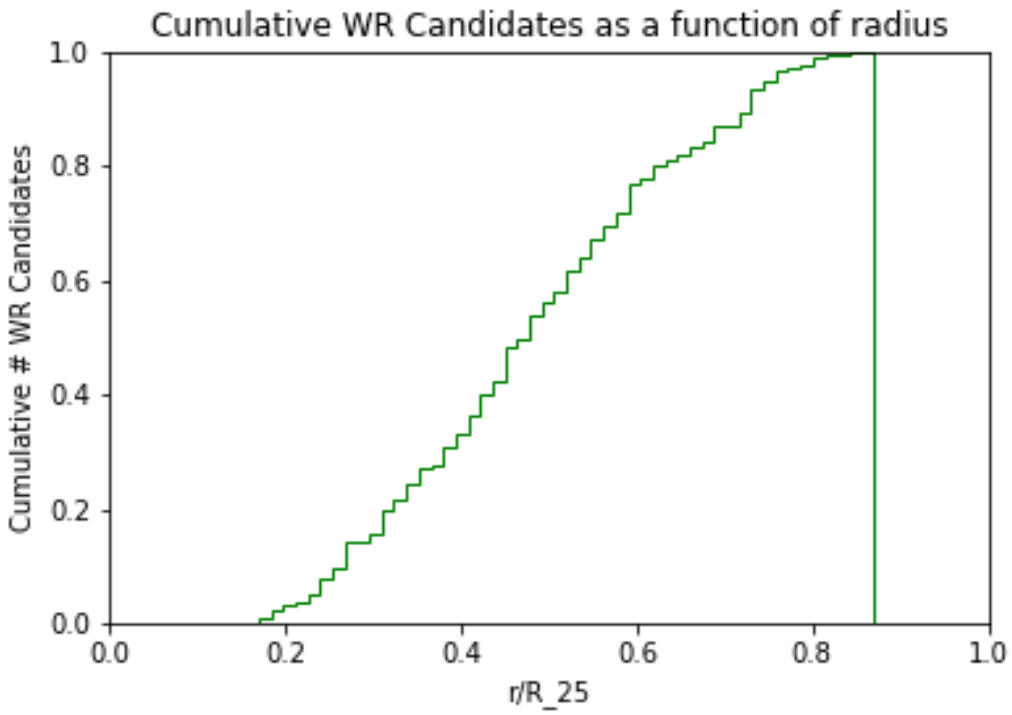

Figure 4.2: The cumulative fraction of WR candidates from my BSc thesis over deprojected radius (Sharp, 2020). The radius starts at 0.2 r/R_{25} because the center of the galaxy is too bright and crowded to identify HeII excesses and finishes at 0.8 r/R_{25} because only the central 95 percent of the galaxy fit into the VLT FORS1 FoV.

4.1.1 Type ratios

As expected from the intermediate to high metallicity, the confirmed WR stars within NGC6744 have a near even WC to WN ratio of 18 WN to 17 WC stars. However, does this split reflect the actual ratio within the galaxy? The narrow band continuum subtraction method of finding WR candidates is biased towards finding WC stars as they tend to have greater HeII excesses. Especially given the spatial resolution of this data, there is certainly a population of WR stars in this galaxy that have not been detected and it would be assumed that a greater proportion of these stars are WN than WC.

Conversely, as discussed later on in Section 4.4, the two surveys I compare this survey to had a greater number of WC stars than WN stars in their spectroscopically confirmed WR stars. Compared to these galaxies, NGC6744 has fewer WC stars than expected. If this is not an observation bias, then potentially NGC6744 is generally lower in metallicity than measured.

Alternatively, this could be a result of different selection biases. Different surveys use different telescopes and instruments, which will affect the data in various ways. For the survey of NGC5068, the telescope and instrument were the same. However, the selection bias is not identical as the smaller distance to NGC5068 means fewer WR stars will be diluted by higher spatial resolution (Pledger et al., 2021). Conversely, both the M101 and Milky Way surveys used multiple instruments, which makes comparison even more difficult, as the biases may not be consistent across the whole survey.

4.2 HII Regions

Eighty-six percent of the spectra that contained WR features also displayed nebular Hα, implying they are found within HII regions. As the spatial resolution of this data is quite poor, this cannot confirm all these stars are physically within the HII regions. Higher resolution imaging would be able to determine how many of these sources are actually

within the HII regions and how many are only associated with them due to poor spatial resolution.

Three of the brighter HII regions in this survey are also identified as infrared sources by Yew et al. (2018). M05 S07 and M05 S20 have positions consistent with radio emitting HII regions. M05 S24 is 1" (50pc) separated from a radio emitting HII region. This radio emission is produced by bremsstrahlung radiation. This is evidence of a significant amount of ionisation from massive stars, which produces bremsstrahlung radiation when recombining. For 2 of these regions, M05 S20 and M05 S24, WR features were detected but the high continuum luminosities of these regions and clear underlying stellar populations made it difficult to determine what emission was from the WR and what was from other stars so an estimate of the WR population within these regions was not made.

4.3 Metallicity

There is an offset between the O3N2 metallicity gradient and the N2 metallicity gradient found by this work, however, they agree within error. In Marino et al. (2013) a similar offset is found, however, they do not investigate this directly, instead comparing their measurements to a calibration that uses both $N2/R2$ and $S2/R2$ ratios from Pilyugin et al. (2010). For the O3N2 relation this offset is 0.02dex, where the electron temperature (T_e) derived abundances are larger. The N2 calibration is offset by 0.08dex, where the T_e derived abundances are larger as for the N2 calibration. Given that my values agree within error, there is no implication that this offset is evident in this data but better S/N and spatial resolution could confirm this.

Neither of the 2 metallicity calibrations I used take into account the ionisation factor of the HII region. I used the equations from Marino et al. (2013) based upon the strong line methods first presented in Pettini & Pagel (2004). Lopez-Sanchez et al. (2012) find that the Pettini & Pagel (2004) metallicity calibrations demonstrate an error of 0.25 dex due to ionisation factors. While this paper did not investigate the updated Marino et al.

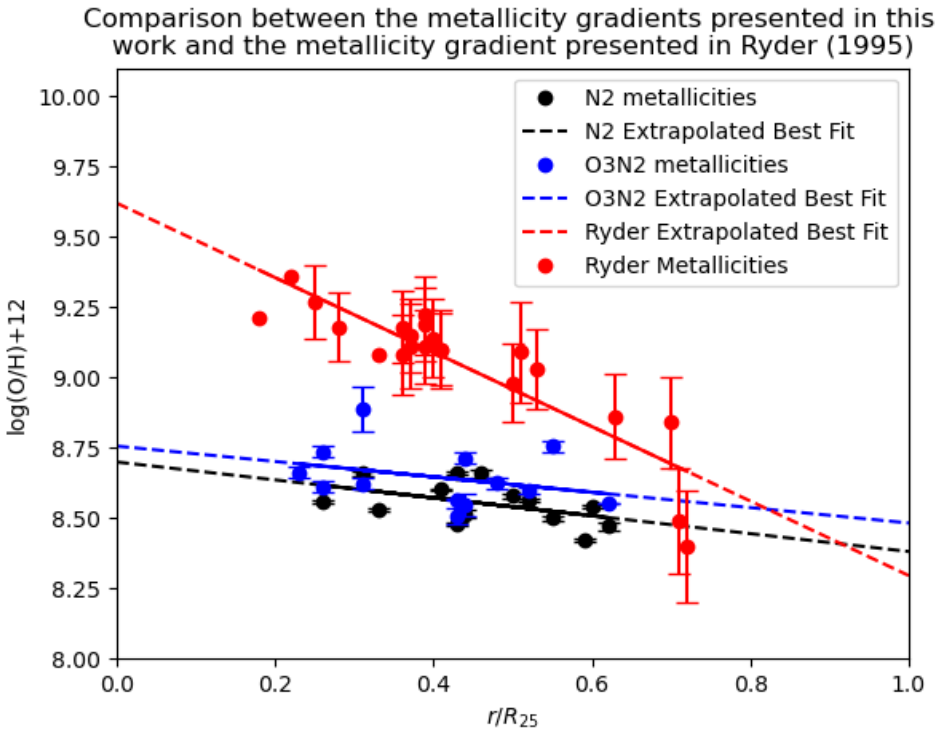

Figure 4.3: The metallicity gradients presented earlier in this thesis have been plotted against the values given in Ryder (1995). The line of best fit was determined with a least squares fit.

(2013) equations, Marino et al. (2013) calculate their calibration from a best fit to their data and do not directly investigate the effect of ionisation. Therefore, ionisation effects may still be affecting the results, especially given that WR stars are known to ionise the regions around them. To investigate this would require data with good enough S/N that weak lined methods could be used to measure T_e which is more directly linked to metallicity.

4.3.1 Metallicity Gradient

Ryder (1995) find the metallicity gradient of NGC6744 to be $-1.31 \pm 0.26 dex/R_{25}$. As shown in Figure 4.3, I found a shallower gradient of $-0.3 \pm 0.06 dex/R_{25}$. However, all my data is from the South East of the galaxy and I did not measure the central metallicity or the

metallicity of the outermost regions. Additionally, I focused on regions with strong HeII emission which may have been enriched by the products of local massive star formation and not be accurate outside of these regions.

Another explanation for the difference is that Ryder uses a R_{23} calibration method, rather than the O3N2 and N2 methods I used. The R_{23} method is known to be double valued and could have skewed their results.

The conflict between these results warrants further investigation in future.

4.4 Comparison to other galaxies

4.4.1 M101

M101 is a giant ScI spiral galaxy with a steep metallicity gradient, transitioning from a near solar metallicity of $O/H + 12 = 8.8$ to a sub solar metallicity of $O/H + 12 = 7.5$ in the outermost regions. It is predicted to have a SFR between $1.7 M_{\odot} yr^{-1}$ and $3.3 M_{\odot} yr^{-1}$ which is comparable to that of NGC6744 (Pledger et al., 2018). Pledger et al. (2018) confirm 11 WC stars and 4 WN stars spectroscopically, which is very different to my ratio of 17 WC to 18 WN despite NGC6744 being only slightly less metal rich. However, this may be due to the fact that I only extracted spectra from the mask containing fainter targets, which are more likely to be WN stars due to the interference filter technique used to select targets.

Poor spatial resolution prevented fainter and isolated WR stars within M101 from being found. Pledger et al. (2018) had access to KPNO, Gemini and HST data and showed that in the poorer resolution KPNO data the number of WR stars in HII regions was estimated at 70 percent, whereas in the HST data it was estimated 50 percent of the WR stars were within HII regions. As Pledger et al. (2018) only spectroscopically confirmed 10 WR sources the statistics are not reliable enough to apply to this survey, but if the trend is confirmed in follow up surveys then it can be assumed that the percentage of WR stars

found within HII regions in NGC6744 is an upper limit.

4.4.2 NGC5068

NGC5068 is an SAB(rs)cd spiral galaxy with central metallicity $Log(O/H) + 12 \sim 8.74$. Its SFR is much lower than NGC6744 at $0.63^{+0.11}_{-0.13} M_{\odot} yr^{-1}$(Bibby & Crowther, 2012). It has a stellar mass of $2.51 \times 10^9 M_{\odot}$ (Tonry et al., 2001). Bibby & Crowther (2012) find 30 WR sources containing 18 WN stars and 24 WC stars spectroscopically and infer a further 43 WN stars and 11 WC stars from photometry. They estimate the global WR population in this galaxy is $\sim$ 170. While other works have found greater metallicity in the central regions of NGC6744, I have found a central metallicity of 8.73 ± 0.06, which is approximately equal to that of NGC5068. NGC5068 is forming stars at a much slower rate than NGC6744, this would suggest that NGC6744 should have a greater number of WR stars but a similar ratio of WN to WC stars. My WN to WC ratio does not agree with the ratios of WN to WC stars presented by Bibby & Crowther (2012). However, my catalogue contains only stars from the longest exposure mask, generally fainter stars, and therefore may have an overrepresented population of WN stars. I also have not inferred any WR stars from photometry, which would likely add a greater number of WN stars than WC stars to the list.

Bibby & Crowther (2012) find a metallicity gradient in NGC5068 of $logO/H + 12 = (8.74 \pm 0.15) - (0.61 \pm 0.22) r/R25$. Interestingly, while Ryder (1995) found a steep gradient for NGC6744, their gradient for NGC5068 was much shallower, at $logO/H + 12 = (8.96 \pm 0.12) - (0.35 \pm 0.26) r/R25$. This is the opposite to NGC6744, which has a steep gradient in Ryder (1995) and a shallower gradient presented in this work. All but one of the data points in Ryder (1995) are between 0.2 and 0.7 r/R_{25}, with one point at around 0.1 r/R_{25}. In contrast, Bibby & Crowther (2012) has 3 points between 0.0 and 0.2 r/R_{25} and 6 between 0.7 and 1. The lack of data points between $0.0 - 0.2$ and $0.7 - 1.0 r/R_{25}$ in my own data could be hiding a steeper or shallower gradient than presented in this work.

The Bibby & Crowther (2012) study came out before the Marino et al. (2013) paper updated the N_{II} and $O_{III}N_{II}$ metallicity calculations, and so likely suffers from systematic over-estimation of metallicity in the highest metallicity regions.

4.4.3 Milky Way

Of most interest, however, is the comparison between the Milky Way and NGC6744. Unlike other galaxies, it is beyond our capabilities to observe the Milky Way face on. Observations of stars within our Galaxy must contend with interstellar dust and proper motion. Hence, it is comparatively simpler to observe stellar populations in close by external galaxies. NGC6744 is too distant for ground based imaging to resolve individual WR stars within, however, its theoretical structural similarity to the Milky Way makes it a valuable galaxy for comparison.

Rate et al. (2020) find that between 15 and 41 percent of Galactic WR stars are associated with a star cluster or OB association. This is at odds with my survey, which finds 86 percent of confirmed WR stars in NGC6744 are in HII regions. Potentially this is an effect of spatial resolution. Rate et al., 2020 mention this possibility but are unable to investigate it due to the lack of reliable parallaxes and distances available for Galactic WR stars. This would, however, corroborate the findings of Pledger et al. (2018) in M101. There is the additional consideration that my selection criteria are primarily sensitive to WR stars within HII regions, and not those found in the field.

Chapter 5

Conclusion

I have carried out spectroscopy of sources within NGC6744 to measure metallicity across the galaxy and identify WR stars.

From spectroscopy I present 7 HeII regions containing 35 WR stars, with comparison to Galactic WR templates showing 17 of these to be WC stars and 18 to be WN stars. In addition, 3 objects need to be re-observed to determine their WR properties, due to diagnostic lines falling in chip gaps, and 2 objects require re-examining to calculate the continuum level of the cluster which would then be used to measure an accurate number of the WR stars within.

I also present fluxes for the diagnostic lines observed in 19 of the spectra extracted from Mask 05. These fluxes were used to calculate extinction corrections and metallicities for each observed region. I derive an estimate for the metallicity of $Log(O/H) + 12 = 8.73 - 0.30(\pm 0.06) \times R$ from a mean of the two metallicity gradients calculated. This estimate is valid for values of R between $0.2R_{25} < R < 0.7R_{25}$. To confirm the metallicity measurement observations, observations with better S/N and spatial resolution are needed so that weak line methods can be used to measure metallicity more directly.

I have found that the ratio of confirmed WC to WN stars in my survey is lower than would be expected compared to M101 and NGC5068. This is likely an artificial difference, due to the bias towards fainter stars in the mask I chose to analyse. WN stars are generally

fainter than WC stars and therefore likely make up a greater amount of the WR sources in this mask than the shorter exposure masks observing brighter objects. Analysing the spectra from the two other masks available would likely prove or disprove this hypothesis. I predict these other masks will contain a greater number of WC stars, due to them containing brighter sources, with likely greater HeII excess.

I also find that a greater percentage of my WR sources are associated with HII regions than the Galaxy or M101. This may be an effect of spatial resolution, as both M101 and stars within the Galaxy can be imaged at higher spatial resolution than NGC6744. This can only be proved definitively with higher spatial resolution observations of NGC6744.

Bibliography

Aguilera-Dena D. R., Langer N., Antoniadis J., Pauli D., Dessart L., Vigna-Gómez A., Gräfener G., Yoon S.-C., 2022, Astronomy and Astrophysics, 661, A60

Anand G. S., et al., 2021, Monthly Notices of the Royal Astronomical Society, 501, 3621–3639

Barniske A., Hamann W. R., Gräfener G., 2006, in Lamers H. J. G. L. M., Langer N., Nugis T., Annuk K., eds, Astronomical Society of the Pacific Conference Series Vol. 353, Stellar Evolution at Low Metallicity: Mass Loss, Explosions, Cosmology. p. 243

Beals C. S., 1929, Monthly Notices of the Royal Astronomical Society, 90, 202–212

Bersten M. C., et al., 2014, Astronomical Journal, 148, 68

Bibby J. L., Crowther P. A., 2012, Monthly Notices of the Royal Astronomical Society, 420, 3091–3107

Cao Y., et al., 2013, The Astrophysical Journal, 775, L7

Cardelli J. A., Clayton G. C., Mathis J. S., 1989, Astrophysical Journal, 345, 245

Castor J. I., Abbott D. C., Klein R. I., 1975, The Astrophysical Journal, 195, 157–174

Conti P. S., 1975, Memoires of the Societe Royale des Sciences de Liege, 9, 193–212

Conti P. S., Crowther P. A., Leitherer C., 2008, From luminous hot stars to starburst galaxies. Cambridge astrophysics series, Cambridge University Press, Cambridge, UK. New York, USA

Crowther P. A., 2007, Annual Review of Astronomy and Astrophysics, 45, 177–219

Crowther P. A., De Marco O., Barlow M. J., 1998, Monthly Notices of the Royal Astronomical Society, 296, 367–378

Crowther P. A., Dessart L., Hillier D. J., Abbott J. B., Fullerton A. W., 2002, Astronomy and Astrophysics, 392, 653

Crowther P. A., Morris P. W., Smith J. D., 2006, Astrophysical Journal, 636, 1033

Crowther P. A., Rate G., Bestenlehner J. M., 2023, Monthly Notices of the Royal Astronomical Society, 521, 585–612

Drew J., Barlow M., Unruh Y., Parker Q., Wesson R., Pierce M., Masheder M., Phillipps S., 2004, Monthly Notices of the Royal Astronomical Society, 351, 206

Dsilva K., Shenar T., Sana H., Marchant P., 2020, Astronomy & Astrophysics, 641, A26

Dsilva K., Shenar T., Sana H., Marchant P., 2022, Astronomy & Astrophysics, 664, A93

Dyk S. D. V., et al., 2018, The Astrophysical Journal, 860, 90

Eldridge J. J., Maund J. R., 2016, Monthly Notices of the Royal Astronomical Society: Letters, 461, L117–L121

Eldridge J. J., Fraser M., Smartt S. J., Maund J. R., Crockett R. M., 2013, Monthly Notices of the Royal Astronomical Society, 436, 774–795

Gal-Yam A., et al., 2022, Nature, 601, 201–204

Groh J. H., Georgy C., Ekström S., 2013, Astronomy and Astrophysics, 558, L1

Hadfield L. J., Crowther P. A., 2008, in Bresolin F., Crowther P. A., Puls J., eds, IAU Symposium Vol. 250, Massive Stars as Cosmic Engines. p. 327–332, doi:10.1017/S1743921308020656

Hamann W. R., Gräfener G., Liermann A., 2006, Astronomy and Astrophysics, 457, 1015

Han Z., Podsiadlowski P., Lynas-Gray A., 2010, Astronomy and Astrophysics, Supplement, 329, 41

Heger A., Fryer C. L., Woosley S. E., Langer N., Hartmann D. H., 2003, The Astrophysical Journal, 591, 288–300

Herald J. E., Schulte-Ladbeck R. E., Hillier D. J., 1999, Symposium - International Astronomical Union, 193, 242–243

Kankare E., et al., 2014, Astronomy and Astrophysics, 572, A75

Kennicutt Jr. R. C., 1998, Annual Review of Astron and Astrophys, 36, 189–232

Kennicutt Robert C. J., Lee J. C., Funes J. G., J. S., Sakai S., Akiyama S., 2008, The Astrophysical Journal Supplement Series, 178, 247–279

Kilpatrick C. D., et al., 2018, Monthly Notices of the Royal Astronomical Society, 480, 2072–2084

Kilpatrick C. D., et al., 2021, Monthly Notices of the Royal Astronomical Society, 504, 2073–2093

Koribalski B. S., et al., 2004, The Astronomical Journal, 128, 16–46

Lang P., et al., 2020, The Astrophysical Journal, 897, 122

Larsen S. S., Richtler T., 1999, Astronomy and Astrophysics, 345, 59

Lopez-Sanchez A. R., Dopita M. A., Kewley L. J., Zahid H. J., Nicholls D. C., Scharwächter J., 2012, Monthly Notices of the Royal Astronomical Society, 426, 2630–2651

Maeder A., 1996, in Vreux J. M., Detal A., Fraipont-Caro D., Gosset E., Rauw G., eds, Liege International Astrophysical Colloquia Vol. 33, Liege International Astrophysical Colloquia. p. 39

Maeder A., Conti P. S., 1994, Annual Review of Astronomy and Astrophysics, 32, 227–275

Marino R. A., et al., 2013, Astronomy & Astrophysics, 559, A114

Modjaz M., 2011, Astronomische Nachrichten, 332, 434–447

Moens N., Poniatowski L. G., Hennicker L., Sundqvist J. O., Mellah I. E., Kee N. D., 2022, arXiv:2203.01108 [astro-ph]

Morton D. C., 1967, The Astrophysical Journal, 147, 1017

Neugent K., Massey P., 2019, Galaxies, 7, 74

Neugent K. F., Massey P., Morrell N., 2018, Astrophysical Journal, 863, 181

Pettini M., Pagel B. E. J., 2004, Monthly Notices of the RAS, 348, L59

Pilyugin L. S., Thuan T. X., Vilchez J. M., 2006, Monthly Notices of the Royal Astronomical Society, 367, 1139–1146

Pilyugin L. S., Vílchez J. M., Thuan T. X., 2010, The Astrophysical Journal, 720, 1738–1751

Pledger J. L., Shara M. M., Wilde M., Crowther P. A., Long K. S., Zurek D., Moffat A. F. J., 2018, Monthly Notices of the Royal Astronomical Society, 473, 148–164

Pledger J. L., Sharp A. J., Sansom A. E., 2021, Monthly Notices of the Royal Astronomical Society, 503, 2168–2178

Rate G., Crowther P. A., Parker R. J., 2020, Monthly Notices of the RAS, 495, 1209

Ryder S. D., 1995, The Astrophysical Journal, 444, 610

Sabbi E., et al., 2018, Astrophysical Journal, Supplement, 235, 23

Saffer R. A., Bergeron P., Koester D., Liebert J., 1994, Astrophysical Journal, 432, 351

Sana H., et al., 2012, Science, 337, 444–446

Sander A. A. C., 2022, arXiv e-prints, p. arXiv:2209.00312

Shara M. M., Bibby J. L., Zurek D., Crowther P. A., Moffat A. F. J., Drissen L., 2013, The Astronomical Journal, 146, 162

Sharp A. J., 2020, Bachelors, University of Central Lancashire

Shenar T., Gilkis A., Vink J. S., Sana H., Sander A. A. C., 2020, Astronomy and Astrophysics, 634, A79

Silva P. d., Steiner J. E., Menezes R. B., 2018, The Astrophysical Journal, 861, 83

Smith L. J., Willis A. J., 1982, Monthly Notices of the Royal Astronomical Society, 201, 451–472

Smith L. J., Crowther P. A., Prinja R. K., 1994, Astronomy and Astrophysics, 281, 833–854

Smith L. F., Shara M. M., Moffat A. F. J., 1996, Monthly Notices of the Royal Astronomical Society, 281, 163–191

Tonry J. L., Dressler A., Blakeslee J. P., Ajhar E. A., Fletcher A. B., Luppino G. A., Metzger M. R., Moore C. B., 2001, Astrophysical Journal, 546, 681

Van Dyk S. D., 2017, Philosophical Transactions of the Royal Society of London Series A, 375, 20160277

Vink J. S., 2022, Annual Review of Astronomy and Astrophysics, 60, annurev

Walborn N. R., 1991, in Haynes R., Milne D., eds, Proceedings of the Symposium of the IAU Vol. 148, The Magellanic Clouds. p. 145

Yew M., et al., 2018, Publications of the Astronomical Society of Australia, 35

Yusof N., et al., 2013, Monthly Notices of the Royal Astronomical Society, 433, 1114–1132

de Vaucouleurs G., de Vaucouleurs A., Corwin Herold G. J., Buta R. J., Paturel G., Fouque P., 1991, Third Reference Catalogue of Bright Galaxies. Springer New York, https://ui.adsabs.harvard.edu/abs/1991rc3..book.....D

van der Hucht K. A., 2001, New Astronomy Reviews, 45, 135–232

van der Hucht K. A., Conti P. S., Lundstrom I., Stenholm B., 1981, Space Science Reviews, 28, 227–306

Appendix A

BSc WR candidates list

In this chapter I present the WR candidates list from my BSc thesis Sharp (2020). It consists of three multipage tables.

Table A.1: Table of candidates selected by Blinkgrade program

ID	RA	Dec	HeII mag	err	HeII6 mag	err	HeII6-HeII	err
1	19:09:36.957	-63:48:07.971	23.24	0.03	23.50	0.04	0.26	0.05
2	19:09:39.601	-63:48:35.849	21.78	0.01	21.88	0.01	0.09	0.02
3	19:10:10.464	-63:50:14.658	23.28	0.06	23.53	0.05	0.25	0.08
4	19:09:32.799	-63:53:38.754	23.21	0.09	24.88	0.18	1.67	0.20
5	19:09:18.580	-63:52:25.048	22.74	0.04	23.44	0.04	0.70	0.05
6	19:10:03.991	-63:50:23.920	23.34	0.05	24.01	0.06	0.67	0.08
7	19:10:12.100	-63:49:26.486	23.26	0.04	24.82	0.07	1.56	0.08
8	19:10:12.830	-63:49:38.519	22.73	0.06	23.10	0.04	0.38	0.07
9	19:10:02.308	-63:53:41.374	23.76	0.06	25.69	0.25	1.93	0.26
10	19:10:09.199	-63:52:14.180	23.00	0.03	23.71	0.06	0.70	0.07
11	19:10:11.849	-63:52:48.196	23.27	0.04	24.16	0.09	0.88	0.10
12	19:09:18.414	-63:54:12.470	23.08	0.05	23.43	0.07	0.35	0.08

Continued on next page

Table of candidates selected by Blinkgrade program.

ID	RA	Dec	HeII mag	err	HeII6 mag	err	HeII6-HeII	err
13	19:09:57.613	-63:50:35.572	21.15	0.06	21.62	0.07	0.48	0.09
14	19:09:57.613	-63:50:35.572	21.15	0.06	22.08	0.06	0.93	0.09
15	19:09:31.341	-63:49:08.104	22.83	0.07	23.39	0.09	0.55	0.11
16	19:09:38.690	-63:49:35.333	22.96	0.04	23.39	0.08	0.43	0.09
17	19:09:16.921	-63:49:43.408	23.55	0.02	24.31	0.04	0.76	0.05
18	19:09:23.981	-63:49:46.235	22.08	0.12	22.77	0.08	0.70	0.14
19	19:10:10.305	-63:49:47.743	22.18	0.13	22.89	0.07	0.72	0.15
20	19:10:04.796	-63:50:19.181	23.03	0.04	24.31	0.14	1.28	0.15
21	19:10:03.079	-63:53:13.344	23.16	0.05	23.46	0.07	0.30	0.09
22	19:09:18.927	-63:53:21.851	23.01	0.06	23.45	0.07	0.45	0.09
23	19:09:41.598	-63:53:46.854	22.97	0.04	24.26	0.16	1.29	0.16
24	19:09:41.598	-63:53:46.854	22.97	0.04	23.79	0.09	0.81	0.10

Continued on next page

Table of candidates selected by Blinkgrade program.

ID	RA	Dec	HeII mag	err	HeII6 mag	err	HeII6-HeII	err
25	19:09:28.950	-63:54:09.239	23.61	0.06	25.25	0.25	1.65	0.25
26	19:10:00.860	-63:54:35.061	21.77	0.05	22.07	0.03	0.30	0.06
27	19:09:21.840	-63:48:43.709	22.11	0.07	22.36	0.04	0.26	0.08
28	19:09:57.668	-63:49:04.036	22.95	0.03	23.35	0.03	0.39	0.04
29	19:09:27.819	-63:49:51.114	23.53	0.03	25.32	0.13	1.8	0.13
30	19:09:28.904	-63:51:11.069	23.30	0.05	24.22	0.08	0.92	0.10
31	19:10:14.940	-63:52:33.769	23.55	0.07	24.31	0.11	0.76	0.13
32	19:09:17.106	-63:51:40.232	22.10	0.05	22.72	0.05	0.63	0.07
33	19:09:21.157	-63:52:24.320	23.23	0.05	23.92	0.08	0.69	0.09
34	19:10:03.335	-63:53:10.506	22.88	0.08	24.58	0.14	1.70	0.16
35	19:10:04.515	-63:53:17.073	23.13	0.06	24.89	0.17	1.75	0.18
36	19:09:51.892	-63:54:37.036	23.23	0.06	24.03	0.12	0.79	0.14

Continued on next page

Table of candidates selected by Blinkgrade program.

ID	RA	Dec	HeII mag	err	HeII6 mag	err	HeII6-HeII	err
37	19:09:54.157	-63:54:36.673	22.65	0.03	23.26	0.04	0.61	0.05
38	19:09:22.265	-63:51:22.963	21.62	0.05	21.97	0.06	0.35	0.08
39	19:09:33.843	-63:51:40.641	20.98	0.13	21.80	0.05	0.83	0.14
40	19:10:07.530	-63:52:30.595	23.25	0.05	24.30	0.12	1.05	0.13
41	19:10:01.144	-63:53:49.682	21.95	0.04	22.22	0.04	0.27	0.06
42	19:10:04.543	-63:50:16.555	19.78	0.06	20.01	0.04	0.22	0.07
43	19:10:11.078	-63:51:43.993	23.09	0.07	23.71	0.11	0.63	0.13
44	19:10:09.263	-63:53:34.242	23.20	0.06	24.39	0.08	1.20	0.10
45	19:09:23.055	-63:50:36.840	23.26	0.08	23.81	0.12	0.55	0.14
46	19:09:58.359	-63:52:57.417	23.22	0.05	23.48	0.06	0.26	0.08
47	19:09:35.224	-63:53:29.541	22.90	0.06	23.53	0.11	0.63	0.12
48	19:09:35.224	-63:53:29.541	22.90	0.06	24.36	0.14	1.47	0.15

Continued on next page

Table of candidates selected by Blinkgrade program.

ID	RA	Dec	HeII mag	err	HeII6 mag	err	HeII6-HeII	err
49	19:09:44.391	-63:53:55.707	23.74	0.06	24.89	0.23	1.15	0.24
50	19:09:49.465	-63:53:57.077	22.78	0.06	23.56	0.09	0.78	0.11
51	19:09:47.568	-63:48:18.745	23.21	0.07	23.49	0.06	0.28	0.09
52	19:09:45.064	-63:49:27.969	21.00	0.05	21.27	0.05	0.27	0.07
53	19:09:44.167	-63:48:24.734	21.76	0.06	22.12	0.07	0.36	0.09
54	19:09:37.172	-63:49:40.525	22.70	0.04	23.07	0.05	0.37	0.07
55	19:09:31.698	-63:50:37.022	22.29	0.03	22.54	0.03	0.25	0.04
56	19:09:43.094	-63:53:09.261	21.42	0.07	21.79	0.07	0.37	0.10
57	19:09:57.775	-63:48:10.371	21.67	0.08	22.10	0.05	0.43	0.10
58	19:09:42.105	-63:49:33.223	21.59	0.09	21.98	0.06	0.38	0.11
59	19:09:38.525	-63:50:41.492	20.61	0.07	20.95	0.05	0.34	0.09
60	19:09:50.303	-63:52:46.342	22.52	0.07	23.40	0.17	0.88	0.19

Continued on next page

Table of candidates selected by Blinkgrade program.

ID	RA	Dec	HeII mag	err	HeII6 mag	err	HeII6-HeII	err
61	19:09:30.789	-63:51:30.320	22.18	0.05	22.58	0.11	0.40	0.12
62	19:09:50.791	-63:52:36.480	22.94	0.07	23.44	0.13	0.50	0.15
63	19:10:09.627	-63:52:44.266	22.79	0.08	23.43	0.08	0.64	0.11
64	19:09:56.435	-63:54:16.162	23.35	0.05	24.39	0.10	1.04	0.11
65	19:10:09.304	-63:49:29.107	21.32	0.07	21.62	0.05	0.3	0.09
66	19:09:37.117	-63:48:06.037	23.48	0.04	23.83	0.05	0.35	0.06
67	19:09:51.798	-63:49:37.719	23.94	0.11	25.19	0.24	1.25	0.27
68	19:09:23.244	-63:50:20.658	20.75	0.06	20.99	0.05	0.24	0.08
69	19:09:40.033	-63:52:24.757	21.77	0.08	22.22	0.05	0.45	0.09
70	19:09:56.489	-63:50:02.586	23.45	0.08	24.57	0.16	1.12	0.17
71	19:09:25.930	-63:49:53.614	21.71	0.09	23.14	0.21	1.43	0.23
72	19:09:20.422	-63:52:24.730	23.82	0.21	25.3	0.26	1.48	0.33

Continued on next page

Table of candidates selected by Blinkgrade program.

ID	RA	Dec	HeII mag	err	HeII6 mag	err	HeII6-HeII	err
73	19:09:50.260	-63:49:49.636	21.66	0.04	21.87	0.06	0.21	0.07
74	19:10:05.040	-63:50:14.077	22.61	0.05	22.92	0.07	0.31	0.09

[p]

Table A.2: Table of candidates with visible brightening in HeII which were selected from the merged star list

ID	RA	Dec	HeII mag	err	HeII6 mag	err	HeII6-HeII	err
75	19:09:15.958	-63:52:38.335	22.35	0.08	22.77	0.06	0.43	0.10
76	19:09:15.840	-63:51:46.826	23.64	0.06	24.56	0.19	0.92	0.20
77	19:09:15.568	-63:48:15.562	24.18	0.04	24.40	0.04	0.21	0.06
78	19:10:16.537	-63:51:28.388	24.21	0.08	24.67	0.10	0.47	0.13
79	19:10:07.558	-63:54:44.626	24.16	0.07	24.66	0.14	0.50	0.15
80	19:10:06.758	-63:54:44.004	22.01	0.04	22.26	0.04	0.25	0.05
81	19:09:51.740	-63:54:46.830	24.29	0.09	24.89	0.17	0.59	0.19
82	19:09:39.329	-63:54:50.341	23.96	0.08	24.99	0.18	1.02	0.19
83	19:09:23.066	-63:54:45.122	21.57	0.13	22.34	0.09	0.77	0.16
84	19:09:24.051	-63:54:47.323	23.85	0.06	23.67	0.04	-0.18	0.08

Continued on next page

Table of candidates with visible brightening in HeII which were selected from the merged star list

ID	RA	Dec	HeII mag	err	HeII6 mag	err	HeII6-HeII	err
85	19:09:46.136	-63:54:52.128	23.76	0.09	23.35	0.09	-0.41	0.13
86	19:09:58.305	-63:54:43.855	24.48	0.10	24.92	0.15	0.44	0.18
87	19:10:07.340	-63:54:38.975	24.10	0.09	24.30	0.10	0.20	0.13
88	19:10:12.699	-63:54:50.312	22.97	0.04	22.89	0.04	-0.09	0.06
89	19:10:13.387	-63:54:30.138	23.09	0.05	22.97	0.09	-0.12	0.10
90	19:10:08.921	-63:54:34.730	21.47	0.06	21.67	0.06	0.19	0.09
91	19:10:08.055	-63:54:24.493	20.61	0.09	20.55	0.06	-0.06	0.11
92	19:10:08.403	-63:54:10.495	22.44	0.05	22.47	0.04	0.03	0.06
93	19:10:02.100	-63:54:17.794	23.86	0.11	23.42	0.08	-0.44	0.13
94	19:09:58.430	-63:54:14.834	22.74	0.06	22.89	0.04	0.15	0.07
95	19:09:49.221	-63:54:24.347	22.37	0.04	22.44	0.03	0.07	0.05

Continued on next page

Table of candidates with visible brightening in HeII which were selected from the merged star list

ID	RA	Dec	HeII mag	err	HeII6 mag	err	HeII6-HeII	err
96	19:09:42.802	-63:54:29.508	22.32	0.04	22.33	0.03	0.01	0.05
97	19:09:39.741	-63:54:20.241	22.20	0.04	22.15	0.03	-0.05	0.05
98	19:09:38.280	-63:54:23.770	23.62	0.15	22.48	0.18	-1.14	0.24
99	19:09:33.837	-63:54:19.948	23.77	0.07	23.56	0.08	-0.22	0.11
100	19:09:23.002	-63:54:16.576	24.15	0.09	24.17	0.10	0.02	0.13
101	19:09:23.336	-63:54:01.749	23.05	0.03	23.00	0.04	-0.04	0.05
102	19:09:35.272	-63:54:10.456	21.82	0.05	21.87	0.04	0.04	0.06
103	19:09:38.506	-63:53:59.015	21.62	0.10	21.44	0.13	-0.17	0.17
104	19:09:49.504	-63:54:00.533	21.31	0.11	21.21	0.11	-0.09	0.16
105	19:10:00.010	-63:54:04.972	24.14	0.08	24.00	0.05	-0.14	0.09
106	19:10:02.864	-63:53:50.357	20.34	0.10	20.23	0.08	-0.11	0.13

Continued on next page

Table of candidates with visible brightening in HeII which were selected from the merged star list

ID	RA	Dec	HeII mag	err	HeII6 mag	err	HeII6-HeII	err
107	19:09:38.088	-63:53:42.974	21.60	0.03	20.83	0.10	-0.77	0.11
108	19:09:26.530	-63:53:43.824	24.51	0.12	24.37	0.09	-0.14	0.15
109	19:09:24.844	-63:53:53.248	22.14	0.03	22.15	0.03	0.01	0.04
110	19:09:16.074	-63:53:50.564	24.07	0.05	24.02	0.05	-0.05	0.08
111	19:09:22.975	-63:53:30.992	22.67	0.10	22.81	0.09	0.14	0.13
112	19:09:26.148	-63:53:20.786	23.81	0.09	23.90	0.06	0.09	0.11
113	19:09:29.775	-63:53:33.171	23.21	0.06	23.20	0.04	-0.01	0.07
114	19:09:37.590	-63:53:41.689	23.40	0.25	22.50	0.03	-0.90	0.26
115	19:09:46.107	-63:53:46.688	22.53	0.05	22.48	0.06	-0.05	0.08
116	19:10:05.547	-63:53:25.232	22.17	0.06	22.08	0.10	-0.09	0.12
117	19:09:54.687	-63:53:16.484	23.01	0.10	22.88	0.09	-0.13	0.13

Continued on next page

Table of candidates with visible brightening in HeII which were selected from the merged star list

ID	RA	Dec	HeII mag	err	HeII6 mag	err	HeII6-HeII	err
118	19:09:43.560	-63:53:15.901	23.68	0.17	23.62	0.14	-0.06	0.22
119	19:09:28.816	-63:53:16.832	21.91	0.03	22.01	0.04	0.10	0.05
120	19:09:27.043	-63:53:10.931	22.30	0.14	21.32	0.12	-0.97	0.19
121	19:09:17.399	-63:53:15.228	23.68	0.09	23.59	0.14	-0.09	0.17
122	19:09:43.985	-63:53:01.393	23.47	0.08	23.81	0.09	0.34	0.12
123	19:09:54.394	-63:52:56.683	22.00	0.08	22.11	0.07	0.11	0.10
124	19:10:05.037	-63:52:49.471	22.78	0.03	22.79	0.03	0.01	0.04
125	19:09:54.887	-63:52:52.822	20.96	0.08	21.11	0.08	0.16	0.11
126	19:09:48.466	-63:52:46.340	23.14	0.15	22.92	0.09	-0.21	0.17
127	19:09:18.689	-63:52:46.033	23.18	0.17	23.07	0.08	-0.11	0.18
128	19:09:18.817	-63:52:49.300	23.48	0.11	23.78	0.10	0.30	0.15

Continued on next page

Table of candidates with visible brightening in HeII which were selected from the merged star list

ID	RA	Dec	HeII mag	err	HeII6 mag	err	HeII6-HeII	err
129	19:09:38.697	-63:52:52.470	21.27	0.12	21.55	0.11	0.28	0.16
130	19:09:52.518	-63:52:54.135	23.06	0.05	22.67	0.07	-0.39	0.09
131	19:10:00.342	-63:53:03.680	22.11	0.08	22.36	0.06	0.25	0.10
132	19:10:00.082	-63:53:05.549	22.87	0.06	23.00	0.09	0.12	0.11
133	19:10:10.523	-63:53:03.164	21.74	0.09	21.67	0.08	-0.07	0.12
134	19:10:11.352	-63:52:56.360	23.63	0.07	23.72	0.08	0.10	0.10
135	19:10:08.621	-63:52:33.815	22.04	0.06	21.82	0.12	-0.22	0.13
136	19:09:54.745	-63:52:33.827	23.98	0.08	24.26	0.12	0.28	0.15
137	19:09:52.538	-63:52:42.193	23.09	0.05	23.14	0.05	0.06	0.08
138	19:09:31.524	-63:52:36.803	21.48	0.09	21.29	0.06	-0.19	0.11
139	19:09:14.615	-63:52:37.825	23.26	0.05	23.24	0.04	-0.02	0.07

Continued on next page

Table of candidates with visible brightening in HeII which were selected from the merged star list

ID	RA	Dec	HeII mag	err	HeII6 mag	err	HeII6-HeII	err
140	19:09:38.292	-63:52:16.723	22.40	0.09	22.57	0.09	0.17	0.13
141	19:10:09.510	-63:52:27.862	22.58	0.04	22.71	0.05	0.12	0.06
142	19:10:10.409	-63:52:23.028	23.53	0.05	23.82	0.09	0.29	0.11
143	19:10:08.094	-63:52:23.430	23.01	0.04	23.20	0.05	0.18	0.07
144	19:10:12.299	-63:52:05.186	23.49	0.09	23.56	0.10	0.07	0.14
145	19:10:04.090	-63:51:55.522	22.68	0.05	22.69	0.05	0.01	0.07
146	19:09:20.028	-63:51:58.809	21.45	0.08	21.64	0.09	0.18	0.12
147	19:09:22.420	-63:51:19.604	21.71	0.12	21.73	0.18	0.02	0.22
148	19:09:17.860	-63:51:17.452	21.16	0.04	21.20	0.03	0.04	0.05
149	19:09:56.008	-63:51:05.161	22.40	0.06	22.62	0.07	0.22	0.09
150	19:09:55.837	-63:51:05.031	22.34	0.11	22.41	0.09	0.07	0.14

Continued on next page

Table of candidates with visible brightening in HeII which were selected from the merged star list

ID	RA	Dec	HeII mag	err	HeII6 mag	err	HeII6-HeII	err
151	19:10:12.134	-63:51:12.483	23.14	0.03	23.11	0.04	-0.02	0.04
152	19:09:21.405	-63:50:38.006	22.88	0.11	23.04	0.14	0.16	0.18
153	19:09:56.908	-63:50:33.573	23.46	0.10	23.52	0.14	0.06	0.17
154	19:09:59.036	-63:50:10.601	23.12	0.05	23.27	0.06	0.15	0.08
155	19:09:56.243	-63:50:23.467	22.45	0.09	22.74	0.07	0.28	0.11
156	19:09:23.292	-63:50:22.129	21.21	0.08	21.40	0.09	0.18	0.12
157	19:09:19.859	-63:50:26.817	23.67	0.06	23.80	0.07	0.13	0.09
158	19:09:26.818	-63:50:02.875	23.26	0.06	23.21	0.06	-0.05	0.09
159	19:09:30.127	-63:50:06.462	22.92	0.07	23.18	0.08	0.26	0.11
160	19:09:53.880	-63:49:52.955	21.77	0.09	21.83	0.10	0.06	0.13
161	19:10:06.521	-63:49:45.316	24.19	0.10	24.23	0.10	0.04	0.14

Continued on next page

Table of candidates with visible brightening in HeII which were selected from the merged star list

ID	RA	Dec	HeII mag	err	HeII6 mag	err	HeII6-HeII	err
162	19:10:00.612	-63:49:50.870	23.58	0.09	23.47	0.09	-0.12	0.13
163	19:09:37.374	-63:49:39.499	23.37	0.06	23.65	0.09	0.28	0.11
164	19:09:21.929	-63:49:49.189	23.47	0.06	23.41	0.11	-0.05	0.12
165	19:09:33.701	-63:49:31.581	22.77	0.05	22.95	0.06	0.18	0.07
166	19:09:39.500	-63:49:27.393	21.68	0.05	21.85	0.06	0.17	0.08
167	19:09:41.734	-63:49:22.346	22.20	0.15	22.44	0.12	0.24	0.19
168	19:09:41.683	-63:49:21.435	22.68	0.10	22.75	0.10	0.06	0.14
169	19:09:59.923	-63:48:59.948	23.05	0.05	23.15	0.05	0.10	0.07
170	19:09:56.787	-63:49:18.165	22.28	0.07	22.53	0.09	0.25	0.12
171	19:09:52.643	-63:49:12.511	23.93	0.06	23.98	0.13	0.05	0.14
172	19:09:50.198	-63:49:10.501	23.30	0.07	23.49	0.06	0.20	0.09

Continued on next page

Table of candidates with visible brightening in HeII which were selected from the merged star list

ID	RA	Dec	HeII mag	err	HeII6 mag	err	HeII6-HeII	err
173	19:09:38.949	-63:49:06.259	23.84	0.09	24.09	0.07	0.25	0.12
174	19:09:25.698	-63:49:13.773	23.88	0.04	23.90	0.03	0.02	0.05
175	19:09:58.107	-63:48:41.563	23.50	0.07	23.73	0.06	0.23	0.09
176	19:10:08.280	-63:48:39.799	22.49	0.03	22.57	0.03	0.08	0.04
177	19:09:15.603	-63:48:23.812	22.52	0.02	22.54	0.02	0.02	0.03
178	19:09:18.479	-63:48:20.351	22.24	0.02	22.18	0.03	-0.06	0.03
179	19:09:34.234	-63:48:20.099	22.72	0.11	22.96	0.10	0.24	0.15
180	19:09:37.522	-63:48:14.669	24.81	0.05	24.87	0.06	0.06	0.08
181	19:09:57.240	-63:48:02.413	23.49	0.07	23.65	0.10	0.16	0.12
182	19:09:44.137	-63:47:57.980	22.08	0.03	22.17	0.03	0.09	0.04
183	19:09:41.190	-63:47:59.078	21.98	0.01	22.06	0.01	0.07	0.02

Table A.3: Table of candidates selected from visible difference between the HeII and the HeII6 image but which don't have photometry

ID	RA	Dec
184	19:09:39.180	-63:54:41.59
185	19:09:38.405	-63:54:49.65
186	19:09:50.266	-63:54:43.88
187	19:10:01.522	-63:54:36.87
188	19:10:06.588	-63:54:47.05
189	19:10:14.231	-63:54:40.08
190	19:09:29.258	-63:54:27.25
191	19:09:32.854	-63:53:52.72
192	19:10:04.902	-63:53:51.54
193	19:09:43.889	-63:53:52.03
194	19:09:18.888	-63:53:36.22
195	19:09:17.821	-63:53:24.91
196	19:09:43.086	-63:53:37.10
197	19:09:58.892	-63:53:38.56
198	19:10:08.481	-63:53:35.75
199	19:10:08.030	-63:53:31.90
200	19:10:15.947	-63:53:37.27
201	19:10:06.697	-63:53:18.49
202	19:10:05.316	-63:53:23.31
203	19:10:05.389	-63:53:24.73
204	19:10:03.061	-63:53:26.12

Continued on next page

Table of candidates selected from visible difference between the HeII and the HeII6 image but which don't have photometry

ID	RA	Dec
205	19:09:56.913	-63:53:17.53
206	19:09:49.430	-63:53:26.23
207	19:09:43.530	-63:53:28.40
208	19:09:17.834	-63:53:24.91
209	19:09:40.383	-63:53:02.03
210	19:09:54.543	-63:53:01.63
211	19:09:57.596	-63:52:56.73
212	19:10:11.658	-63:52:45.32
213	19:10:00.554	-63:52.49.36
214	19:09:57.590	-63:52:56.90
215	19:09:57.805	-63:52:51.29
216	19:09:45.465	-63:52:51.38
217	19:09:34.957	-63:52:43.80
218	19:09:28.723	-63:52:46.26
219	19:09:18.823	-63:52:43.00
220	19:09:18.462	-63:52:42.37
221	19:09:18.367	-63:52:43.25
222	19:09:40.503	-63:53:02.70
223	19:09:45.439	-63:52:51.25
224	19:10:06.023	-63:52:59.08
225	19:10:05.115	-63:52:50.47

Continued on next page

Table of candidates selected from visible difference between the HeII and the HeII6 image but which don't have photometry

ID	RA	Dec
226	19:10:11.671	-63:52:45.15
227	19:10:09.110	-63:52:34.63
228	19:10:07.819	-63:52:44.01
229	19:10:05.134	-63:52:50.30
230	19:09:34.963	-63:52:43.80
231	19:09:28.723	-63:52:46.34
232	19:09:18.585	-63:52:31.71
233	19:09:19:416	-63:52:32.51
234	19:09:21.464	-63:52:21.75
235	19:09:20.881	-63:52:22.95
236	19:09:56.182	-63:52:20.30
237	19:10:00.443	-63:52:11.63
238	19:10:09.252	-63:52:17.73
239	19:10:07.168	-63:52:09.42
240	19:09:59.949	-63:52:05.73
241	19:09:16.671	-63:51:44.07
242	19:09:16.567	-63:51:33.03
243	19:09:29.708	-63:51:32.77
244	19:10:03.093	-63:51:54.14
245	19:09:37.400	-63:51:22.37
246	19:09:22.649	-63:51:15.21

Continued on next page

Table of candidates selected from visible difference between the HeII and the HeII6 image but which don't have photometry

ID	RA	Dec
247	19:09:22.811	-63:51:23.16
248	19:09:22.199	-63:51:16.96
249	19:09:29.568	-63:51:03.69
250	19:09:30.593	-63:51:05.54
251	19:09:33.224	-63:51:16.48
252	19:09:36.750	-63:50:28.02
253	19:09:25.518	-63:50:15.13
254	19:09:23.441	-63:50:25.27
255	19:09:34.375	-63:50:02.66
256	19:10:00.260	-63:50:00.02
257	19:10:13.383	-63:49:32.66
258	19:10:12.553	-63:49:50.49
259	19:10:12.127	-63:49:43.51
260	19:09:45.476	-63:49:43.22
261	19:09:32.861	-63:49:43.61
262	19:09:30.203	-63:49:22.25
263	19:09:30.898	-63:49:28.28
264	19:09:45.881	-63:49:23.52
265	19:09:45.420	-63:49:23.43
266	19:10:08.578	-63:49:30.19
267	19:10:13.383	-63:49:32.70

Continued on next page

Table of candidates selected from visible difference between the HeII and the HeII6 image but which don't have photometry

ID	RA	Dec
268	19:10:03.523	-63:49:00.86
269	19:09:56.153	-63:49:02.06
270	19:09:15.858	-63:48:49.41
271	19:09:51.539	-63:48:49.64
272	19:09:55.255	-63:48:44.36
273	19:10:03.523	-63:49:00.77
274	19:09:44.576	-63:48:25.03
275	19:09:40.512	-63:48:38.99
276	19:09:48.254	-63:48:07.64
277	19:09:56.947	-63:48:21.35
278	19:09:47.762	-63:48:02.95
279	19:09:39.847	-63:47:55.81